



**HAL**  
open science

## Crack growth behavior in dissimilar welded Ti based alloys under biaxial fatigue loading

Manon Abecassis, Alain Köster, Vladimir A. Esin, Vincent Chiaruttini,  
Vincent Maurel

► **To cite this version:**

Manon Abecassis, Alain Köster, Vladimir A. Esin, Vincent Chiaruttini, Vincent Maurel. Crack growth behavior in dissimilar welded Ti based alloys under biaxial fatigue loading. *International Journal of Fatigue*, 2018, pp.209-224. 10.1016/j.ijfatigue.2018.09.013 . hal-01883371

**HAL Id: hal-01883371**

**<https://hal.science/hal-01883371>**

Submitted on 28 Sep 2018

**HAL** is a multi-disciplinary open access archive for the deposit and dissemination of scientific research documents, whether they are published or not. The documents may come from teaching and research institutions in France or abroad, or from public or private research centers.

L'archive ouverte pluridisciplinaire **HAL**, est destinée au dépôt et à la diffusion de documents scientifiques de niveau recherche, publiés ou non, émanant des établissements d'enseignement et de recherche français ou étrangers, des laboratoires publics ou privés.

# Crack Growth Behavior in Dissimilar Welded Ti Based Alloys under Biaxial Fatigue Loading

M. Abecassis<sup>a</sup>, A. Köster<sup>a</sup>, V. A. Esin<sup>a</sup>, V. Chiaruttini<sup>b</sup>, V. Maurel<sup>a,1</sup>

<sup>a</sup>*MINES ParisTech, PSL Research University, MAT - Centre des Matériaux, CNRS UMR 7633, BP 87 91003 Evry, France*

<sup>b</sup>*Onera, Université Paris-Saclay, Materials and Structures Department, 29 av Division Leclerc 92320 Châtillon, France*

---

## Abstract

This study aims at describing fatigue crack growth in dissimilar welding of Ti based alloys under macroscopic multiaxial loading. The proposed methodology involves the experimental analysis of fatigue crack behavior under equibiaxial tension and macroscopic combination of mode I and II for Ti17, Ti6242 and laser welded specimen of both base metals. Based on these experiments, crack path, fatigue crack growth rate and crack interaction with microstructure have been addressed. The 3D finite element analysis of cracks shapes has enabled to derive stress intensity factor (SIF) investigated for opening, in-plane and out-of-plane shear modes based on linear elastic fracture mechanics assumptions. Finally, an equivalent SIF has been proposed to take into account the local mode mixity induced by both macroscopic shear and 3D crack shape. As a conclusion, the dissimilar welding of Ti based alloys increase the fatigue crack growth rate (FCGR) for any macroscopic loading - with or without shear. Moreover, the microstructure of Ti6242 alloy, is well known to inhibit FCGR by multiples local bifurcation of crack path induced by the coarse microstructure of this alloy. This point was confirmed during equibiaxial tension but anomalous and very high FCGR was observed for macroscopic mode I + II loading. For the welded material, the fatigue crack to microstructure interactions have shown that the FCGR was clearly limited by coarse  $\alpha$  needles inducing local bifurcation and conversely that in both fusion zone and heat-affected zone, local refinement of  $\alpha$  needles could not slow down the crack propagation.

*Keywords:* laser welding, Ti17 alloy, Ti6242 alloy, macroscopic shear fatigue, crack and microstructure interactions, J-integral, Paris law, In situ observation

---

<sup>\*</sup>Corresponding author. Tel.: +33-1-60 76 30 03; Fax: +33-1-60 76 31 50  
E-mail address: vincent.maurel@mines-paristech.fr

## Highlights

- Biaxial fatigue crack growth tests are carried out for Ti17, Ti6242, and welded specimen
- FCGR is the highest for welded specimen and the lowest for Ti6242 for equibiaxial tension
- Fatigue crack is not inhibited by microstructure in Ti6242 alloy for macroscopic mode I + II
- SIF in mode I, II and III is derived from 3D FEA of relevant crack shape
- An equivalent SIF is proposed to account for mode mixity

## 1. Introduction

Due to their exceptional mechanical properties for a moderate density, Ti based alloys have a very wide range of applications from medical implant to aeronautical and nuclear components, from low to high temperature. In order to optimize the design of critical mechanical components and even reduce safety factors, robust damage tolerance approaches must be involved [1]. In case of intense fatigue loading, fatigue crack growth should be addressed. In this respect, the assessment of fatigue crack growth rate (FCGR) is required. For Ti based alloys, FCGR is particularly sensitive to the microstructure refinement [2]. Furthermore, it is well established that the fatigue crack path in Ti based alloys depends on the crystallographic structure: cracks propagate along the prismatic, pyramidal and basal planes of the hexagonal close-packed crystal lattice of  $\alpha$  colonies, which constitute the typical microstructure of these alloys [3, 4]. Besides, elastic anisotropy of  $\alpha$  colonies also impacts their local behavior as a function of their orientation [5, 6]. Thus, a coarse microstructure including a large size of  $\alpha$  colonies would lead to many crack bifurcations. As a major result of these bifurcations, it has also been observed that for fatigue in mode I, an increase in crack bifurcation events enables to decrease the crack growth rate [7, 8, 9]. Besides, for many Ti based alloys, the fatigue crack growth depends on  $\beta$  (and prior  $\beta$ ) grain size which could strongly impact fatigue crack path and associated FCGR [10, 11].  $\beta$  and prior  $\beta$  grains boundaries appear in some cases as additional barrier to crack growth and thus are assumed to lower FCGR [12].

For some parts, welding of dissimilar alloys used as base metals can be required depending on the specifics of each grade accounting for mechanical properties, economic consideration or design complexity. Nevertheless, the welding is known to lead to a modification of mechanical properties of the base metal (BM). This modification is mainly the consequence, during the welding process, of the strong impact of the heating on the microstructure in both the fusion zone (FZ) and heat affected zone (HAZ). For example, for ferritic and austenitic stainless steels, the crack growth within the fusion zone or the HAZ are observed to induce higher fatigue crack growth rate, than that originally measured on the base metal, both for constant stress intensity factor (SIF) amplitude and for stress controlled experiments [13, 14].

The extreme sensitivity of the fatigue crack growth to the microstructure of Ti based alloys makes their welding a challenging issue. On the one hand, for friction welded Ti17 alloy, the highest FCGR is observed in the fusion zone, and the lowest one in the base metal for CT specimens [15]. Authors stress out that the FCGR increase was induced by the brittle behavior of a locally harder material than the base metal [15]. On the other hand, for dissimilar welding between Ti17 and Ti-6Al-4V, the fatigue lifetime, for strain controlled tests, was governed by new detrimental  $\alpha'$  and  $\alpha''$  martensitic phases. These phases were observed to be located along the electron beam, between the welded joint and the subsequent local points of low hardness where cracks initiate [16].

Considering the FCGR analysis in the Paris regime, the influence of a multiaxial loading is of great concern. Indeed, for many components in various applications, the local loading evolves in orientation, intensity, and multiaxiality during the crack growth. This is due to the complexity of the local geometry where a crack could initiate and grow. Thus, the mode mixity induced by a local multiaxial loading must be taken into account. In this respect, some equivalent SIFs -  $\Delta K_{eq}$  - have been proposed to model the evolution of FCGR according to mode mixity and have been widely commented [17, 18, 19, 20]. But a general analytical expression of  $\Delta K_{eq}$  could not be obtained and is still a point to be addressed. The limitation of some  $\Delta K_{eq}$  models could be a dependency to the tested material [21], an oversimplification of mode mixity (due to the use of handbook for SIF analysis) or the strong influence of the complexity of the loading path [22]. Besides, an increasing number of commercial finite element analysis (FEA) codes enable the computation of local mode mixity, using X-FEM [23], mesh-less method [24] or conform remeshing technique [25]. Subsequently, the quality of an equivalent SIF should be evaluated to provide a clear guidelines in its use.

In order to carry out a test under multiaxial loading, a fatigue testing with a modification of the notch orientation to the loading direction could drive locally mode I+II [26, 14]. Ding et al [27] have proposed to use a plate with multiple holes, leading sequentially to mode I and mode I + II, which induce crack bifurcations. However, for these two cases, only the design of the specimen prescribes the mode mixity, thus it could finally lead to a rather low sensitivity of the FCGR within limited mode mixity [26]. To tackle such difficulties, a biaxial coplanar device directly allows a mode mixity control to observe crack bifurcation and the associated FCGR [28, 29].

Therefore, the aim of this paper is to determine experimentally the influence of the welding on the FCGR for a laser welding of dissimilar Ti based alloys under macroscopic equibiaxial and combined mode I and II fatigue loading. Because the real crack path impacts the mode mixity, the three dimensional geometry of the crack path would be analyzed experimentally. Moreover, while an evolution of the microstructure induced by the welding process and an extreme sensitivity of the FCGR to the microstructure of the Ti based alloys are expected, a special attention will be paid to these aspects. Both

Table 1: Chemical composition (wt. %) of Ti17 and Ti6242 alloys used in the present study

Element	Al	Sn	Zr	Mo	Cr	O	Si	Ti
Ti17	4.54	2.10	2.06	3.91	3.93	<0.13	0.06	Bal.
Ti6242	5.72	2.09	3.95	1.86	0.01	<0.15	0.1	Bal.

Ti17 and Ti6242 alloys are used as base metals and are tested in the same conditions, to be compared to the welded material, addressing the analysis of the microstructure influence on crack behavior. Then, an equivalent SIF to account for mode mixity is finally proposed. This task has been carried out using an explicit meshing of the 3D crack path obtained experimentally.

## 2. Materials and methods

Two different titanium alloys, Ti17 and Ti6242 as well as their assembly obtained by laser beam welding, provided by Safran Aircraft Engines, were used in this study. The alloys have been received as disks of 100 mm in diameter and 3 mm in thickness obtained by a forging process.

### 2.1. Microstructure characterization of the base metals

The chemical compositions of Ti17 and Ti6242 alloys are given in Table 1. A difference in Zr, Mo and Cr content was observed. The microstructure was revealed by chemical etching using a Kroll solution (2 ml HF, 3 ml HNO<sub>3</sub>, 95 ml H<sub>2</sub>O).

Ti17 is a  $\beta$ -rich  $\alpha - \beta$  Ti based alloy whereas Ti6242 is a near- $\alpha$  Ti based alloy. The microstructure of both alloys consists of colonies of  $\alpha$  needles located in prior  $\beta$  grains, Figure 1(a) and Figure 1(b). The size of prior  $\beta$  grains in Ti17 alloy was obtained by a linear intercept method in different cross-sections relative to the direction of forging, orthogonal to the observed cross-sections. Ti17 alloy has equiaxed prior  $\beta$  grains in the direction of forging with an average diameter of 800  $\mu\text{m}$  and elongated grains in the cross-section orthogonal to the direction of forging with an average length of 750  $\mu\text{m}$  and width of 420  $\mu\text{m}$ .  $\alpha$  needles are embedded in the  $\beta$  matrix, Figure 1(a). The used etching technique did not allow us to reveal clearly the prior  $\beta$  grains in Ti6242 alloy and thus  $\beta$  grains size cannot be measured. The length and thickness of  $\alpha$  needles have been measured by intercept method. For Ti17, the average length and thickness were about 3 and 0.4  $\mu\text{m}$  respectively. For Ti6242, the average length and thickness were about 92 and 3  $\mu\text{m}$  respectively, see details in Table 2.

### 2.2. Microstructure characterization of the welded specimen

Both forged disks of Ti17 and Ti6242 alloys were cut along one diameter, chamfered and then welded by laser beam. To achieve a better welding quality, the half disks were partially machined to reduce the thickness in the centre corresponding to the final gauge area of the specimen (described in section

Table 2: Average values of length and thickness of  $\alpha$  needles corresponding for welded material to Figure 2; the arrows indicate the observed gradient measured along the direction from the center of the FZ to the BM (see text for details).

		Length ( $\mu m$ )	Thickness( $\mu m$ )
Ti17		2.8 $\pm$ 1.7	0.4 $\pm$ 0.2
Ti6242		92. $\pm$ 27.	3.0 $\pm$ 1.0
Fusion Zone		1.0 $\rightarrow$ 2.0 $\pm$ 0.2	-
HAZ-Ti17		2.0 $\rightarrow$ 2.7 $\pm$ 0.1	-
Welded Specimen	HAZ-Ti6242 "secondary"	1.0 $\pm$ 0.1	0.15 0.2
	HAZ-Ti6242 "primary"	100. $\pm$ 10.	7 $\pm$ 0.2

2.3). In order to relax residual stresses induced by the welding process, an annealing was carried out at 606 °C during 8 hours followed by air-cooling, before further machining. Because the microstructure of Ti based alloys is very sensitive to thermal treatment [30, 31, 32, 33], it should be carefully analyzed for the welded specimen to determine the actual microstructure induced by both welding and final thermal treatment. The  $\beta$  transus of Ti17, of 890 °C (resp. 995 °C for Ti6242), has been exceeded in the HAZ. However the location of this area is not easy to find in the welded specimen, because it is not obvious to determine only by SEM or chemical measurements the points where transus has been exceeded.

The microstructure of the welded specimen was characterized by optical microscopy (OM) and Scanning Electron Microscopy (SEM). A cross-section of the welded sample is shown in Figure 1(c), where different macroscopic zones have been defined. In this figure, the red lines delineate the final gauge area location obtained after machining of the sample. To obtain a clear understanding of the impact of the welding on microstructure, detailed views of different areas of the welded specimen have been presented in Figure 2. Five areas can be distinguished and accordingly the details of the microstructure are:

- The fusion zone (FZ) located at the centre of the welded joint, which resulted from the fusion of Ti17 and Ti6242 alloys during the welding process. At this location, the chemical composition, Figure 1(d), appeared to be intermediate between those of each base metal, whereas, the hardness reached here a maximum value, Figure 1(e). The local maximum of hardness corresponded to the most refined microstructure associated to the smallest size of  $\alpha$  needles, see Figure 2 (a) and (f) and corresponding measurements in Table 2;
- Base metals (BM), Ti17 and Ti6242, located at approximately 2 mm far from the centre of the welded joint, where the initial microstructures were observed. The composition, Figure 1(d), the hardness, Figure 1(e), values and the microstructure, Figure 2 (e) and (j) and Table 2, observed in these areas corresponded to those of initial Ti17 and Ti6242 alloys;
- Heat-affected zones (HAZ) observed between base metals and FZ. In the sequel, the HAZ between the fusion zone and the Ti17 base alloy (resp. Ti6242 base alloy) is referred to as HAZ-Ti17 (resp. HAZ-Ti6242). It is worth noting that within HAZ the chemical composition was close to

the associated base metal, Figure 1(d), whereas the hardness was significantly higher, Figure 1(e). Moreover, together with the observed decrease of hardness from the FZ to HAZ, Figure 1(e), the size of  $\alpha$  needles was observed to increase, Figure 2. Within HAZ-Ti6242, two different populations of  $\alpha$  needles have been revealed: primary  $\alpha$  needles much bigger than secondary  $\alpha$  needles, Figure 2(i) and Table 2.

The length and thickness of  $\alpha$  needles in the welded specimen have been reported in Table 2. Because of the gradient of the microstructure induced by the welding process, average length and thickness have been given from the center of the FZ to the BM. For some areas, because of the very small size of  $\alpha$  needles, and of the high signal to noise ratio, it was rather difficult to ascertain their thickness. In this case, only the lengths of  $\alpha$  needles have been given in Table 2. However, these measurements have confirmed that  $\alpha$  needles have been refined in the FZ and their size progressively increased to the BMs through the HAZs

### 2.3. Specimen geometry

Cross-shaped specimens were processed by Electro Discharge Machining (EDM), Figure 3. A central hole and two notches were machined as well by EDM at the centre of the specimen within the gauge area of the reduced section of 1 mm in thickness, see Figure 3(b) and (c) and red lines in Figure 1(c). The notches were aligned with the direction of one of the bisector between the two loading axis, Figure 3(a). For the welded specimen, the welded joint and the notches were parallel. The misalignment,  $\Delta$ , between the bisector and the welded joint was about 500  $\mu\text{m}$  (see red dashed line in Figure 3(b)). In addition to cross-shaped specimen, a CT specimen was used to identify FCGR in Ti17 alloy. In this case the CT specimen was obtained from the same initial material as used for cross-shape specimen. The CT specimen used in this case was a so-called CT16, its dimensions were  $b = 5$  mm,  $w = 32$  mm and  $h = 38$  mm.

### 2.4. Experimental procedure

To obtain FCGR reference curve under pure mode I, basic fatigue crack propagation tests have been achieved for base-metals. Fatigue crack propagation tests for Ti17 were performed at room temperature with CT16 specimens, on an Instron 8502 hydraulic fatigue machine, using a 50 kN cell force. The force varied according to a sinusoidal function at 1Hz with a constant amplitude  $F_{\text{max}} = 1.95$  kN. Fatigue crack propagation test for Ti6242 were performed at room temperature with SENT specimens, on the same facility, at 1Hz. The crack length was continuously measured by the potential drop technique. Details of this test can be found in [34].

Fatigue crack propagation tests with cross-shape specimen were performed on an Instron 8800 planar biaxial hydraulic fatigue device with 4 orthogonal actuators. Each actuator bears a maximum load of 100 kN and a maximum displacement of  $\pm 20$  mm. Biaxial fatigue crack growth tests were carried out

at room temperature and force controlled; the force varied according to a sinusoidal function with a constant amplitude  $F_{\max}$  at a frequency of 1Hz; the load ratio was set to  $R=0.1$ . The biaxial loading ratio,  $T$ , was defined as the ratio between the maximum loads  $F_{2,\max}$  and  $F_{1,\max}$  applied respectively along Axis #2 and Axis #1:

$$T = \frac{F_{2,\max}}{F_{1,\max}} \quad (1)$$

Initially, the maximum force were equal in both directions,  $F_{2,\max} = F_{1,\max}$ , and were set to 5 kN. Thus, the macroscopic combination of mode I and II was controlled by lowering  $F_{2,\max}$  and keeping  $F_{1,\max}$  as a constant value. The macroscopic loading was defined by the value of the parameter  $T$ . Each test consisted of three steps:

1. Crack initiation and propagation under equibiaxial loading in tension ( $T=1$ ). The transition between this step and step (2) started when the observed crack increment was about  $800 \mu m$ . The projected length on the bisector between directions 1 and 2 of the crack was accounted for to obtain simple in situ measurement, Figure 3(a);
2. Progressive crack bifurcation with a decreasing load along Axis #2 in successive steps ( $T=0.9$  then  $T=0.8$ ). This step of progressive bifurcation was required to avoid any other crack initiation from the notch. Each of these sub-steps was limited either by 10,000 cycles or by a propagation of  $200 \mu m$  of the crack length obtained by potential drop technique measurement, see welded probes in Figure 5. That is to say that, as soon as one of these two criteria was reached, the step was assumed to be ended. As a direct consequence, the crack growth of these steps has differed for each test;
3. Crack propagation combining macroscopic shear and opening modes, leading to mode I+II ( $T=0.7$ ).

These three steps have been detailed in Table 3.

Table 3: Loading steps

Step	T	$F_{1,\max}$ (kN)	$F_{1,\min}$ (kN)	$F_{2,\max}$ (kN)	$F_{2,\min}$ (kN)
Equibiaxial	1.			5.	0.5
Bifurcation	0.9	5	0.5	4.5	0.45
	0.8			4.	0.4
Macroscopic mode I and II	0.7			4.25	0.5

Probably due to some current loss associated to the shape of the specimen, it has been observed that the sensitivity of the potential drop technique was rather low and was not relevant to measure crack bifurcation. This was the reason why all subsequent analysis have been performed using optical measurements of the crack location.

An optical numerical microscope Keyence® VHX 2000 was used to measure in situ crack length and path, on one side of the specimen. Due to the complexity of the crack path, the crack length  $a$  was evaluated through its curvilinear length measurement deduced from surface optical images and subsequent image analysis. The crack length was obtained for each crack branch and included the half-length of the notch, considering long crack analysis. The crack growth rate was derived from the ratio of a constant increment of crack length  $\Delta a \simeq 50 \mu\text{m}$  and the corresponding increment of cycles  $\Delta N$  :

$$\frac{da}{dN} \simeq \frac{\Delta a}{\Delta N} \quad (2)$$

We introduced two angles that should be seen as a macroscopic description of the crack path. The angle of bifurcation, described by the so-called tilt angle  $\theta$  in the sequel, was evaluated as the angle between the crack path for  $T=1$  and the crack path for  $T=0.7$  accounting for the final position of the crack, Figure 4(a). The angle induced by the flat to slant transition of the crack, described by the so-called twist angle  $\psi$  in the sequel, was evaluated as the angle between the crack from side to side of the specimen for a given position of the crack, Figure 4(b). These measurements were obtained assuming the same location of crack tip on each side of the specimen.

After fatigue tests, the gauge area of the specimen containing the notch and cracks was extracted by EDM from the specimen. The obtained disk was cut down to  $800 \mu\text{m}$  ahead of each crack tip. Specimen were cooled with liquid nitrogen and mechanically opened by uniaxial tension. Ex situ surface observations have been achieved with a LEO 1450VP SEM.

### 3. Experimental Results

#### 3.1. Crack path analysis

Some major crack branches are observed in situ, Figure 5. They have been respectively distinguished as Crack #1 and Crack #2 in the sequel. During the first stage ( $T=1$ ), the crack path was mostly parallel to the notch direction (i.e. parallel to the direction of one bisector of the specimen). During the biaxial loading ratio evolution from  $T=1$  to  $T=0.7$ , a progressive global crack bifurcation has been observed on all tested specimens, so that the cracks tend to get perpendicular to the local maximum stress direction [27, 28]. For Ti17 and welded specimen, the observed crack bifurcation was progressive during the evolution of the biaxial loading ratio, Figure 5(a) and 5(c). For Ti6242, the crack path was complex and irregular, leading to a global bifurcation not as progressive as the one observed for the Ti17 specimen after changing the loading conditions, Figure 5(b). Measurements of tilt angles,  $\theta$ , have been summarized in Table 4 for each one of the tested materials: tilt angles values  $\theta$ , were higher for Ti6242 than those measured for welded and Ti17 specimens, while the smallest  $\theta$  angles having been reached for

Ti17.

Table 4: Tilt angles  $\theta$  measured for each crack on all specimens at the final locations of cracks resulting from biaxial testing

	Crack #1	Crack#2
Ti17	34°	36°
Ti6242	43°	51°
welded Ti17/Ti6242	27°	40°

At a more local scale, cracks observed in Ti17 base alloy were continuous and regular, Figure 5(a). Whereas for Ti6242 specimen, cracks have exhibited large path oscillations due to local bifurcations, Figure 5(b). For welded specimen, Crack #2 propagating from the welded joint to Ti17 base metal was as regular as observed for Ti17, compare Figure 5(a) and 5(c). Nevertheless, for the welded specimen, Crack #1 propagating to Ti6242 base alloy has presented local bifurcations of much lower amplitude than those observed for BM-Ti6242 specimen, compare Figure 5(b) and 5(c).

Based on surface crack path analysis, the macroscopic twist angle,  $\psi$ , as defined in Figure 4(b), has been determined for each crack branch, Figure 6. For Ti17, Figure 6(a), twist angle was slightly evolving during the stage of equibiaxial loading,  $T=1$ , for both crack branches. Then the twist angle reached a maximum absolute value, 17°, and a maximum amplitude of variation as compared to the initial twist angle, 23°, when macroscopic loading went to 0.7 for Crack #2, evolution referred as  $\psi_2$  in Figure 6(a). For the same specimen, the twist angle was close to 10° for Crack #1 for  $T$  lower than 0.9. For Ti6242 specimen, Figure 6(b), twist angles were oscillating and reached maximum absolute value of 36° for Crack #2 referred as  $\psi_2$ , when macroscopic loading equalled 0.7. The magnitude of peak to peak twist angle for Crack #1 referred as  $\psi_1$  was about 35° from  $T=1$  to  $T=0.7$ . Besides, for Crack #1, absolute value of  $\psi_1$  was lower than 10° for  $T=0.7$  along approximately 1 mm of crack growth. For welded specimen, Figure 6 (c), crack fronts can be considered to be almost perpendicular to the surface except when  $T$  was evolving from 0.8 to 0.7 for Crack #2 growing to Ti17. However, twist angles have remained lower for welded specimen than for Ti17 and Ti6242.

### 3.2. Crack Interaction with Microstructure

For Ti17, SEM observations have confirmed that the crack path was very smooth, see Figure 7(a) where crack path is highlighted by white arrows. With this contrast,  $\alpha$  needles were observed as bright small particles and prior  $\beta$  grains boundaries were observed as bright lines. Therefore, neither influence of  $\alpha$  needles nor influence of prior  $\beta$  grains boundaries has been observed on surface crack paths. For Ti6242, local bifurcation and crack branching were associated to the orientation of  $\alpha$  needles colony as shown in inverse pole figure obtained by EBSD, Figure 7(b). Cracks were observed to propagate along or close to perpendicular directions to these colonies without significant preferential orientation of the

crack. However, no evidence has been found of any influence of prior  $\beta$  grains boundaries on crack paths for Ti6242. These observations have been achieved consistently for the whole crack path and thus for any of the macroscopic loading conditions.

For the welded specimen, due to the position of the notch, Crack #1 initiated at the interface between the fusion zone and the HAZ-Ti6242, and then evolved through the HAZ-Ti6242. Crack#2 initiated in the fusion zone and then grew to the HAZ-Ti17, Figure 7(c). For both branches, the crack paths did not present as significant local bifurcations as for the Ti6242 specimen.

After specimen opening, SEM observations have been carried out in order to analyze the local behavior of the crack, Figure 8 and Figure 9. In these figures,  $x$  denotes the abscissa, i.e. the distance from the notch root in the plane of observation and  $T$  denotes the associated biaxiality ratio, as defined by eq. 1.

For Ti17, fatigue rivers have been initiated from the notch and were observed to the end of the propagation, Figure 8(a). The surface was relatively smooth according to the SEM observation. At a local scale, ductile failure was evidenced by dimples induced by plastic deformation of the  $\beta$  phase, Figure 8(c) [16, 35]. The combination of smooth surface and local dimples should be the result of transgranular cracking, dominating the fatigue crack growth mechanism for Ti17. However, measurements of the twist angle has shown that the flat to slant transition was lower but of the same order of magnitude than the one observed for Ti6242 Figure 6(a) and (b). At some points, the surface has presented a break in continuity through the thickness (e.g. see label 1 in Figure 8(a)). These discontinuities are associated with the local maximum twist and could be the consequences of large slant of the crack leading to roof-top like crack [21]. It could also be associated to the role of a prior  $\beta$  grain boundary. Nevertheless, this kind of event was seldom observed for Ti17 alloy in this study.

For Ti6242 alloy, Figure 8(b), the crack surface has exhibited strong profile variations for small crack extent as compared to Ti17 alloy. The fatigue rivers were still observed for Ti6242, Figure 8(d), but, due to crack discontinuities, they were remarkably shorter than those of the Ti17 alloy. Moreover, crystallographic facets were seen in  $\alpha$  needles characterized by a cleavage-like fracture, Figure 8(d), dominating the fatigue crack growth mechanism for Ti6242, as observed by [35]. Some micro-cracks have been also observed along the crack, Figure 8(d). For this specimen, the complexity of the crack path revealed by fractographic observation, has made unclear the role of the  $\beta$  grain boundaries in such a situation.

The increase of macroscopic shear, indicated by T ratio values above Figure 8(a) and Figure 8(b), has not led to any evidence of modification in crack morphology for both Ti17 and Ti6242.

For the welded specimen, on the one hand, the Crack #2 was evolving in the fusion zone for most of the propagation and in the HAZ-Ti17 close to the end of the crack growth, Figure 9(a). Meanwhile, the loading was varying from  $T=1$  to 0.7 within the fusion zone and the loading has already been established

to  $T=0.7$  when the crack has reached the HAZ-Ti17, see indicative values of  $T$  ratio above the Figure 9(a). For this crack, fatigue rivers and crack front were also revealed, Figs 9(a) and 9(b). For  $T$  varying from 0.9 to 0.8, an intergranular fracture was observed, Figure 9(b) corresponding to label 1 in Figure 9(a). Considering the transition between the fusion zone and the HAZ-Ti17, label 2 Figure 9(a), a difference of crack propagation behavior has been observed although the biaxial ratio was the same: when crack was growing through the HAZ, it became transgranular, Figure 9(c).

On the other hand, the Crack #1 was first propagating at the interface between the fusion zone and the HAZ-Ti6242, Figure 9(a) and 9(d). The fracture surface has exhibited transition between the fusion zone and the HAZ-Ti6242, for which the crack was smoother in the FZ than in the HAZ-Ti6242, Figure 9(d). Some pores have also been observed mainly within the fusion zone and along the interface between fusion zone and HAZ, but their interaction with the crack growth are not obvious, Figure 9(a).

As a partial conclusion on crack growth mechanisms, the observations detailed above were consistent for both external surface and fractographic analysis. For Ti17, the crack was smooth and regular for both surface and volume analysis. Some exceptions were associated to a local break of continuity when maximum twist angles were observed. For Ti6242, the coarse microstructure of  $\alpha$  needles has led to bifurcations, consistent in size, with the length of  $\alpha$  needles and/or  $\alpha$  needles colonies. However, only for the welded specimen, the surface crack appeared to be smooth, using fractographic observations. These observations have shown that, within the FZ, transgranular to intergranular cracking could be induced by macroscopic combination of mode I and II, and that the crack behavior was similar in HAZ-Ti17 (resp. HAZ-Ti6242) as compared to the relative BM-Ti17 (resp. BM-Ti6242). Besides, no evidence of crack closure has been observed, since the crack roughness was not seen to have been modified by severe contact.

#### 4. Modeling Fatigue Crack Growth Rates

The stress intensity factor (SIF) in the case of uniaxial test using standard specimen can be evaluated by handbook, addressing the corresponding shape function, for many standard specimen geometries and loadings [36]. But for biaxial testing, using a non-standard specimen geometry and complex prescribed loadings, a similar approach was not possible. Moreover, experimental results revealed very complex 3D crack geometries, making the analysis of SIF and SIF influence on FCGR a prerequisite to a reliable model development [37]. In this respect, a complementary numerical modeling study has been carried out using the Z-set finite element analysis suite. This software is an implicit general purpose finite element solver, developed at both Ecole des Mines ParisTech and Onera. It allows to perform numerical simulations from microstructure up to complex structures scales, with highly nonlinear material models, using multithreaded computations and a parallel domain decomposition solver. It also includes advanced adap-

tive remeshing techniques (based on INRIA’s Meshgems meshing toolbox <http://www.meshgems.com>), efficient domain integral post-processing and mesh transfer algorithms, used for 3D crack propagation simulations.

#### *4.1. Meshing Technique and Modeling Assumptions*

To take into consideration the influence of crack shape on FCGR, meshing of a relevant crack geometry was a key point. The appropriate meshing was achieved following three steps: i) analysis of crack paths on specimen surfaces, ii) construction of a 3D mesh based on experimental crack path and iii) inserting this surface mesh into the specimen mesh using 3D conform remeshing technique [25].

The first step has been addressed by direct observations of crack path on both sides of the specimen, e.g. Figure 10(a). A polynomial approximation of order 2 to 5 was used to represent the crack path, see Figures 10(b) and 10(c) for Ti17 and Ti6242 respectively (plot for one side of the specimen only). This choice has led to a fairly good representation of the crack path avoiding complexity induced by high order polynomial approximation or high level of mesh refinement needed to represent in details the local crack path, Figure 10(c). The step ii) was obtained by deforming an initial rectangular mesh sized to the orthogonal projection of the crack path. This deformation was obtained on the basis of previous polynomial function modeling the surface crack path and a linear interpolation between each side of the specimen. The crack front was assumed to be straight; many different sizes and position of the initial rectangular mesh were used, in order to model different crack front location and subsequent crack length. Final step iii) was obtained by conform remeshing technique where mesh was refined around the crack front to obtain an accurate analysis of energy release rate by domain integral [38, 39].

Concerning the discretization of the cracked specimen, an automatized four stage approach was performed. The first one, was to extract from a given finite element input file, all the required geometrical entities where boundary conditions have been prescribed, and to generate a surface boundary mesh preserving both required geometrical groups and material regions limits (in a subset of the overall mesh close to the crack surface). Thus, the second stage was carried out using a robust surface to surface intersection algorithm, in order to insert the provided crack mesh, that produced a resulting surface conform triangulation. The third step, was to perform successively adaptive surface remeshing, volume Delaunay triangulation, and adaptive volume remeshing, in order to generate a refined mesh, suitable for both finite element computation and domain integral post-processing. Finally, the last stage consisted in rebuilding a finite element input file of the cracked domain with updated boundary conditions and material domain specifications. Such an adaptive remeshing approach can be applied to any kind of finite element solver (Abaqus or ANSYS for instance, Z-set [40] for the present study).

As an example, the case of Ti6242 was represented on top of Figure 10(d) using the superposition of colored sets of element contiguous to the crack path on the in situ image of the crack path. The perspective

view of the crack was presented on the bottom of Figure 10(d) using one of the sets of elements contiguous to the crack (corresponding to the red subset of elements). This meshing methodology has been applied for Ti17, Ti6242 and welded specimens.

The specimen was modeled using 3D linear elements. The minimum mesh size was set to 100  $\mu m$ . The number of degrees of freedom was about 100,000, varying of less than 3% depending on the crack length. The loading axes corresponded respectively to directions #1 and #2. The thickness of the specimen corresponded to the direction #3. The gauge surface was parallel to the 1-2 plane, Figure 10(e).

For the sake of simplicity, linear elastic fracture mechanics assumptions will be considered. Thus, the material behavior has been described by linear elasticity, considering homogenous properties for the whole specimen. As a first approach, the welded specimen has also been considered homogenous. This basic assumption was motivated by the relatively small variation of the Young modulus between Ti17 and Ti6242, 112 and 114 GPa respectively [41, 42], and the average chemical composition observed within the welded zone, see Figure 1. Moreover, residual stresses have been neglected, since a heat treatment was applied to relax stresses (see section 2.2). No contact between crack lips was taken into account. On the basis of a conform remeshing technique, domain integral and interaction integral analysis were performed using the Z-set software, to compute stress intensity factors for modes I, II and III [40].

#### 4.2. Mode I, II and III Stress Intensity Factor Analysis

To illustrate the influences of crack shape and macroscopic loading on SIF values, we have only considered in this section the Ti17 specimen for one crack. This crack corresponded to the one of maximum twist angle, Crack #2 Figure 6(a), and presented the highest regularity in crack shape, see negative values for  $x$  and  $y$  in Figure 10(a). Firstly, during equibiaxial loading, mode I has appeared to be quasi-constant along the crack front and much higher than modes II and III, Figure 11(a). Out-of-plane shear mode was also observed to be quasi-constant along the crack front, whereas opening and in-plane shear modes have appeared to reach maximum values alternatively: the higher the mode II was the lower the mode I was, and conversely, the higher the mode I was observed the lower the mode II was, Figure 11(a). This effect was maximal at the surface of the specimen, Figure 11(a). A global analysis of shear mode could be evaluated through an equivalent SIF for shear defined as,  $\Delta K_s$ :

$$\Delta K_s = \sqrt{\Delta K_{II}^2 + \Delta K_{III}^2} \quad (3)$$

When crack length was increasing, the macroscopic loading was evolving sequentially. For crack length below 3 mm, the influence of shear was rather low without significant influence of macroscopic combination of modes I and II loadings, Figure 11(b). Only a slight increase in shear mode has been observed when T equalled 0.8. Whereas for T=0.7 and with a crack length above 3 mm,  $\Delta K_s$  was

significantly increasing, especially when  $\Delta K_I$  decreased consistently with observations made along the crack front, Figure 11(a). The crack transition from flat to slant was certainly a key factor in this statement, since the increase of shear mode was consistent with the increase in twist angle, Figure 6(a). As a rational of this evolution of mode mixity, three mixity angles can be analyzed according to eq. 3 to 5 [43]:

$$\Theta = \arctan \frac{K_{II}}{K_I} \quad (4)$$

$$\Psi = \arctan \frac{K_{III}}{K_I} \quad (5)$$

$$\Phi = \arctan \frac{\sqrt{K_{II}^2 + K_{III}^2}}{K_I} \quad (6)$$

These mixity angles have been plotted as a function of the macroscopic experimental twist angle  $\psi$ , Figure 11(c). When twist angle was close to  $6^\circ$ , mixity angles were increasing together with the macroscopic shear induced by any evolution of T, compare Figures 6(a) and 11(c). For increasing crack lengths and corresponding decreasing values of twist angle (maximum absolute value), mixity angles were correlated to twist angles, with an higher influence of mode III as compared to mode II,  $\Psi > \Theta$ . However, the equivalent shear,  $K_s$ , was able to take into account both shear mode II and shear mode III. These points of maximum sensitivity were associated to T=0.7 and a maximum flat to slant evolution of the crack path.

As a partial conclusion, this SIF analysis has shown that in the case of Ti17, for Crack #2 and a length below 3 mm, there was no strong influence of macroscopic combination of mode I and II loading. Whereas, for crack length above 3 mm, the combination of macroscopic shear and large crack twisting has strongly impacted the local mode mixity.

#### 4.3. Influence of Macroscopic I+II and Local Shear Mode on Fatigue Crack Growth Rates

In the context of linear elastic fracture mechanic (LEFM), the use of an equivalent SIF enables the use of a Paris law identified under pure mode I to cover a large range of mode mixity. A short review of known equivalent SIF has been carried out before addressing the identification of a new equivalent SIF.

##### 4.3.1. Review of Equivalent Stress Intensity Factor

To describe FCGR for long cracks, the Paris law is a direct power law function of the amplitude of SIF under pure mode I:

$$\frac{da}{dN} = C \Delta K_I^m \quad (7)$$

where  $m$  and  $C$  are material parameters.

In the sequel, we limit the analysis of literature to criteria expressed as an equivalent SIF,  $\Delta K_{eq}$ , derived from a polynomial analysis of SIF values for the three modes. The general form of such an equivalent SIF is given by:

$$\Delta K_{eq} = (a\Delta K_I^n + b\Delta K_{II}^n + c\Delta K_{III}^n)^{1/n} \quad (8)$$

where n, a, b and c are the model parameters varying for each equivalent SIF.

To evaluate FCGR under multiaxial loading,  $\Delta K_{eq}$  is used as the driving force and the Paris model yields:

$$\frac{da}{dN} = C\Delta K_{eq}^m \quad (9)$$

Many authors have focused their studies on macroscopic analysis of mode I and mode II influence on FCGR. This is the reason why most criteria neglect mode III when macroscopic loading only implies in plane shear.

Tanaka et al. [17] expressed the equivalent SIF as:

$$\Delta K_{eq} = (\Delta K_I^4 + 8\Delta K_{II}^4)^{1/4} \quad (10)$$

In this case, when adding shear, FCGR is higher than FCGR obtained for pure mode I.

An extension of this model to mode III was proposed by Tanaka et al. [17] and yields to:

$$\Delta K_{eq} = \left( \Delta K_I^4 + 8\Delta K_{II}^4 + \frac{8}{1-\nu}\Delta K_{III}^4 \right)^{1/4} \quad (11)$$

where  $\nu$  corresponds to the Poisson's ratio.

Xiangqiao et al [28] choose the following equation:

$$\Delta K_{eq} = 1/2 \cos(\theta_0/2) [\Delta K_I(1 + \cos \theta_0) - 3\Delta K_{II} \sin \theta_0] \quad (12)$$

where  $\theta_0$  is derived from the maximum tangential stress criterion as the solution of the equation:

$$\Delta K_I \sin \theta + \Delta K_{II}(3 \cos \theta - 1) = 0 \quad (13)$$

It is worth noting that, for any twist angle in the range 0 to 45°, the equivalent SIF amplitude is lower than the pure mode I SIF amplitude. As a consequence of this statement, for any twist angle in this range the FCGR will decrease.

Finally, one important equivalent SIF is derived from the energy release rate G and Irwin relationship,

considering a Poisson ratio equal to zero [18] :

$$\Delta K_{eq} = \sqrt{\Delta K_I^2 + \Delta K_{II}^2 + \Delta K_{III}^2} \quad (14)$$

In this case, the mode II and III have the same influence on FCGR.

#### 4.3.2. Definition of an Equivalent Stress Intensity Factor

Based on the chosen modeling assumptions, the evolutions of mode II and III as a function of the crack length seem to be close to each other. Thus, we have proposed to find a local equivalent SIF,  $\Delta K_{eq}$ , using a simple polynomial expression derived from eq. 8 where  $a$  was set to unity and  $b$  was assumed to be equal to  $c$ ,  $b = c = \alpha$ . This simplification has yielded to the following expression:

$$\Delta K_{eq} = (\Delta K_I^n + \alpha \Delta K_{II}^n + \alpha \Delta K_{III}^n)^{1/n} \quad (15)$$

with  $\alpha$  and  $n$  the model parameters to be identified.

The model identification was carried out using the results for Ti17 due to the regularity of the crack path and the subsequent continuity of FCGR evolution, as compared to Ti6242. The goal was there to obtain for multiaxial loading using  $\Delta K_{eq}$  the same Paris law parameters,  $C$  and  $m$ , as identified under pure mode I fatigue test. The summary of the experimental data has been presented in table 5.

Table 5: Paris law parameters for Ti17 and Ti6242

Material	Paris parameters		Reference	Loading	Specimen
	m	C			
Ti17	2.5	$6.33^{-11}$	this study	pure mode I	CT
Ti17	2.5	$7.34^{-11}$	this study	multiaxial	cross-shape
Ti6242	3.	$1.90^{-11}$	[34]	pure mode I	SENT
Ti6242	3.	$1.24^{-11}$	this study	multiaxial	cross-shape
FZ→Ti17	2.5	$1.38^{-10}$	this study	multiaxial	cross-shape
FZ→Ti6242	3.	$3.74^{-11}$	this study	multiaxial	cross-shape

Strong evolutions of SIF for different modes have been observed through the thickness of the specimen, especially on the edge of the specimen, Fig. 11(a). However, edge effect could artifact SIF evaluation. Besides, all SIF evolutions were consistent with each other as a function of the location in the thickness of the specimen, despite some variations from side to side. The use of  $\Delta K_s$  has enabled to limit this variation. Thus, for sake of simplicity, further analysis of SIF amplitude would be limited to the averaged values obtained along the crack front from 3D computations for each mode, namely  $\Delta K_I$ ,  $\Delta K_{II}$  and  $\Delta K_{III}$ . Thus, Figure 12 presents:

- Pure mode I analysis, neglecting mode II and III - namely  $n=1$  and  $\alpha=0$ ,

- Tanaka's model [17], assuming an equivalent influence of mode II and III - namely  $n=4$  and  $\alpha=8$  by setting Poisson coefficient to zero as proposed in [18],
- Forth et al model [18] - namely  $n=2$  and  $\alpha=1$ ,

For both cracks, using a pure mode I description, short crack behavior were observed leading to relatively constant FCGR, then decrease of FCGR and final increase of FCGR for  $\Delta K_I$  ranging from 10 to 15 MPa $\sqrt{m}$ . The decrease of FCGR has been especially observed for Crack #1. Then, for  $\Delta K_I$  above 15 MPa $\sqrt{m}$ , long crack behaviors were observed with continuous increase of FCGR as a function of  $\Delta K_I$  for both cracks, Figure 12.

Considering, Crack #1, the FCGR was not that sensitive to the different tested equivalent SIF. For this crack, obtained FCGR was relatively close to observed FCGR for the CT specimen, for pure mode I. However, for Crack #2, it was obvious that none of the above equivalent SIF was sufficiently sensitive to local mode mixity, so as to reach the Paris law exponent known for pure mode I. This difference of behavior between each crack branch was certainly related to the observed differences in twist angles, see Figure 6(a). This point will be discussed in the sequel.

The new proposed equivalent SIF was identified so as to obtain an optimal correlation of FCGR for biaxial test with results of FCGR for CT specimen under pure mode I. The main goal was to achieve this correlation considering the longest range of cracks, here reached for loading corresponding to the maximum macroscopic shear (mode I + II), namely for  $T=0.7$  and for  $\Delta K_I$  above 15 MPa $\sqrt{m}$ , for the Ti17. An iterative optimization has yielded to  $n=2$  and  $\alpha=8$ . The chosen equivalent SIF was expressed as an equivalent SIF  $\Delta K_{eq}$ :

$$\Delta K_{eq} = (\Delta K_I^2 + 8\Delta K_{II}^2 + 8\Delta K_{III}^2)^{1/2} \quad (16)$$

This new criterion enabled the obtention of a FCGR evolution consistent with results identified on CT specimen with the same material and, besides, a similar FCGR for both cracks. This has resulted in a fairly good approximation of FCGR for multiaxial case considering long crack and Paris domain. The Paris law has been identified for both CT specimen and cross-shape specimen, prescribing the same Paris exponent and based on the proposed expression for  $\Delta K_{eq}$  to analyze multiaxial loading. In Figure 12 straight continuous line and dashed line corresponded respectively with biaxial and CT tests. Finally the  $C$  parameters obtained for CT and biaxial testing were very close to each other, when compared to observed experimental noise for FCGR measurement, see data reported in Table 5.

## 5. Analysis of FCGR for Base Metals and Dissimilar Welding

For validation purpose, the proposed equivalent SIF according to eq. 16 should be applied to tested BM material configurations. A reference curve was obtained from a previous study for Ti6242 alloy [34],

where tests have been achieved using a SENT specimen at a frequency of 1 Hz at room temperature with the same machine than used for CT specimen in the present study. The Ti6242 alloys were in both studies of the same composition and have shown close microstructure features [34].

Average SIF values obtained along the crack front were used for each test, Figure 13. The different colors used for markers correspond to different biaxiality ratio varying from 1 to 0.7 evidencing the capacity of the chosen equivalent SIF to encompass a wide range of macroscopic loading for both crack branches of Ti17, Figure 13(a) and 13(b).

For Ti6242, very high amplitude of oscillations were observed in FCGR evolution as compared to biaxial results obtained for Ti17, Figures 13(c) and 13(d). Despite these oscillations in FCGR, biaxial results were consistent with the reference data obtained in mode I reported as a dashed line in Figures 13(c) and 13(d). Prescribing the exponent obtained for pure mode I to describe the Paris law for biaxial testing, it was observed that FCGR for biaxial loading was consistent to FCGR obtained for pure mode I and  $\Delta K_{eq}$  lower than  $17 \text{ MPa}\sqrt{\text{m}}$  for both crack branches. Nevertheless, attention should be paid for Crack #1, Figure 13(c), where FCGR has reached a maximum value for  $\Delta K_{eq}$  ranging from 16 to  $20 \text{ MPa}\sqrt{\text{m}}$ , and for which the model was seen to be unable to grasp experimental FCGR, this point corresponding to the maximum macroscopic shear loading with  $T=0.7$ . Whereas for Crack #2, Figure 13(d), the experimental FCGR was much lower than when using a Paris law obtained for pure mode I. This point should be discussed further on since for this range of equivalent SIF and for macroscopic combination of mode I and II, the FCGR has appeared to be higher for Ti6242 than for Ti17.

Finally, the proposed equivalent SIF was used to evaluate the FCGR of the welded specimen, Figures 13(e) and 13(f). Paris law identified for base metals under biaxial loading, have been added to Figures 13(e) and 13(f) using straight lines indicated as Ti17 and Ti6242 respectively. The FCGR obtained for the welded specimen was for any crack location, any biaxiality ratio and any  $\Delta K_{eq}$ , the highest FCGR as compared to base metals, Figure 13(e) and 13(f).

Due to the dissymmetry of the welded specimen, it should be kept in mind that Crack #2 has propagated through the fusion zone to the HAZ-Ti17, Figure 13(e), and that Crack #1 has propagated from the interface between the fusion zone and the HAZ-Ti6242 to the HAZ-Ti6242, Figure 13(f). Because of the microstructure gradient, the Paris laws for both Cracks #1 and #2 have been only identified for equibiaxial loading for the welded specimen. This identification was achieved prescribing the Paris law exponent to the value found for each base metal to which cracks were propagating.

The FCGR for Crack #2 increased during the equibiaxial stage of a crack propagating through the fusion zone. When the crack was reaching the HAZ-Ti17, the FCGR had reached the FCGR obtained for Ti17 for  $\Delta K_{eq}$  above  $16 \text{ MPa}\sqrt{\text{m}}$  and  $T$  decreasing from 0.8 to 0.7. Using the exponent value  $m=2.5$

found for BM-Ti17 under mode I, Paris law identified on this crack branch was an upper bound of the FCGR, while the Paris law identified for BM-Ti17 was a lower bound of FCGR.

For Crack #1, the FCGR increased during all the propagation, and has remained close to the Paris law identified with the exponent  $m=3$  found for BM-Ti6242 under mode I, Figure 13(f). However, the FCGR was higher, for this crack branch, than the FCGR of Ti6242 for the whole crack propagation. Moreover, in this case, no clear influence of the transition from fusion zone to the HAZ-Ti6242 has been observed (transition of material corresponds approximately to  $\Delta K_{eq}=12 \text{ MPa}\sqrt{\text{m}}$  and  $T=0.9$ ). The obtained Paris law for Crack#1 in welded specimen has led to an upper bound of experimental FCGR. The FCGR of Ti6242 in base metal Figure 13(c) was a lower bound of FCGR in welded specimen.

## 6. Discussion

The first point addressed by this study was the ranking of the three tested materials in crack propagation under fatigue for equibiaxial, assumed to be pure mode I, and macroscopic combination of mode I and II loadings. The highest FCGR was observed for welded specimen, as compared to base metals. The Ti6242 was the best material under equibiaxial tension, but surprisingly, combining mode I and mode II has led to a large increase in FCGR for a relatively wide range of SIF. Moreover, the crack path sensitivity to the microstructure depended on the alloy, thus each tested material should be considered separately.

For Ti6242, the local crack path deviations were of high amplitude all along the crack path, for crack path oscillations observed on surface, Figures 5(b) and 7(b), as well as for crack oscillations within the bulk of the specimen, Figure 6(b) and 8(d). The amplitude of these oscillations could locally exceed  $100 \mu\text{m}$  in surface. This amplitude was consistent with the length of  $\alpha$  needles observed by SEM, Figure 5 and Table 2. These local crack bifurcations were associated to FCGR oscillations. These observations were fully consistent with previous studies, where authors have shown that the coarser the microstructure of  $\alpha$  needles is, the more the FCGR oscillating is [7], especially in the short fatigue crack regime [44, 45]. However, for long crack behavior, the scatter in FCGR should decrease [7]. This point was not observed in our case for Ti6242: long cracks for macroscopic mode I + II have led to maximum scatter in FCGR. However, the chosen methodology of crack growth measurement, only based on surface optical measurements, could also have magnified the FCGR oscillations.

It could be assumed that for Ti6242 and for any macroscopic biaxial ratio and any crack length, the crack was highly sensitive to the microstructure and was mostly driven by crystallographic features. This point was observed comparing crack path on surface and in volume, Figs. 7(b) and 8(d). This crystallographic cracking clearly had a positive influence for equibiaxial loading, making FCGR in Ti6242 the lowest, but it seemed to be detrimental for macroscopic mode I+II loadings, Figure 13(c) and 13(d).

Nevertheless, neither specific orientation of  $\alpha$  needles nor prior  $\beta$  grains boundary intersecting the crack path were observed. Thus, it could not be claimed that the orientation of colony or prior  $\beta$  grains boundary can explain any FCGR increase. For equibiaxial tension, colonies served as microstructural barrier to crack propagation, but were no longer efficient for large value of biaxiality ratio  $T$  and associated large value of local shear. It can be inferred from these observations that, on the one hand, macroscopic shear loading facilitates intense shear bands and damage in gliding plane selected by local orientation of  $\alpha$  colonies [4]. On the other hand, decrease of FCGR could be induced by non gliding plane localized at the crack tip considering local orientation of loading. At last but not least, it has also been shown by Fessler et al, that for very complex crack tip shapes, crack tip area with local "longer crack" than other areas will induce lower SIF values and subsequently lower FCGR [37]. Alternatively, the "shortest" local crack could induce increase in SIF values and subsequently higher FCGR [37]. Unfortunately, the test set-up prevents from such an analysis.

For Ti17, the crack path was observed to be very smooth and concomitantly the FCGR evolution was observed to be proportional to the crack length, Figure 5(a), 7(a) and 13. Thus, the relatively fine microstructure of  $\alpha$  needles of Ti17, Table 2, was unable to slow down the crack, making the FCGR in Ti17 very high compared to the FCGR in Ti6242. Nevertheless, when macroscopic combination of mode I and II loadings were applied, despite a twist angle magnitude close to the case of Ti6242, FCGR was higher than for pure mode I but without severe acceleration, as observed for Ti6242, Figures 12 and 13. Thus, it could be stated that macroscopic shear loading was less critical for Ti17 than for Ti6242. Moreover, neither the influence of  $\beta$  grains nor the influence of local anisotropy was observed in this study.

For welded Ti17/Ti6242 specimen, the FCGR was clearly the highest, compared to any base metals, Figure 13. When crack reached the HAZ corresponding to one of the base metal, the FCGR reached the value obtained in the base metal tested under the maximum macroscopic shear loading, Figures 13(e) and 13(f). For the tested configurations, crack paths were observed in the welded specimen to be as regular as the crack paths obtained for Ti17, leading to similar crack tilt angles, Table 4. The microstructure of the fusion zone was intermediate in composition between the two base metals.  $\alpha$  needles in fusion zone and HAZ were significantly smaller in size to those measured in Ti17, exhibiting in the HAZ a gradient of  $\alpha$  length and width from the FZ to the BM, Table 2. Thus, again it can be inferred that the fine microstructure of  $\alpha$  needles in the fusion zone and HAZ was unable to slow down the fatigue crack growth.

Since Ti17 alloy has exhibited very low influence of microstructure on both continuity of crack paths and associated regularity of FCGR, this material was very convenient to determine an equivalent SIF within LEFM. This regularity of the crack path has enabled to use simple assumptions for the 3D

modeling of the crack path, based on linear interpolation between surface crack profiles measured on both sides of the specimen. Thus, mode I, II and III were shown to influence the local FCGR and were seen to be straightforward to identify a new equivalent SIF. It is worth noting that for mode II and III the SIF amplitudes were of the same magnitude. Macroscopic in plane combination of mode I and II loading associated with flat to slant evolution of the crack path has led to make both local in-plane and out-of-plane shear modes of equal importance regarding the FCGR. The equivalent SIF proposed in the present work has appeared to be more suitable than already published equivalent SIF. This point is clearly associated by two main points highlighted by the proposed study: firstly, the flat to slant transition has a high impact on local crack behavior, which is seldom analyzed in fatigue and is mainly limited to short crack analysis [46]. Secondly, because most equivalent SIFs minimize the role of shear mode (II or III) for macroscopic mode I+II loading, it seems necessary to amplify the role of shear to assess the observed increase in FCGR. On the basis of this new equivalent SIF, the whole set of materials has been modeled. Nevertheless, this equivalent SIF has only been evaluated for load ratio of  $R=0.1$  and proportional loading in this study.

Because of the microstructure gradient, the Paris law has only been identified for equibiaxial loadings with welded specimen. This identification, together with the observed convergence of FCGR with BM for longest cracks, has led to the upper and lower bounds of FCGR for welded specimen. These bounds, obtained for a same Paris law exponent identified in each BMs, were about a factor 2 on C coefficient of the Paris law eq. 7, see Table 5. For the Crack #1 reaching the BM-Ti6242, it has also been observed that FCGR was very close to the Paris law identified for BM-Ti17. This point could be seen as an additional proof that the refined microstructure found in both HAZ and BM-Ti17 could not prevent high FCGR.

For Ti6242, the modeled  $\Delta K_{eq}$  values were only able to describe relatively low macroscopic mode I + II loadings but has failed to grasp the details of the large increase (and decrease) of FCGR observed to be linked to maximum macroscopic combination of mode I and II loadings. In the assumptions made for crack modeling, the linear interpolation of crack path between each surface could oversimplify the role of shear in the bulk of the specimen: at some points, the macroscopic twist angle was very low, Figure 6(b), whereas the crack roughness was observed to be very high in volume, Figure 8(b). The correlation between large value of macroscopic twist angle and mode mixity angle was shown in Figure 11(c). It can be inferred from these results that local roughness, leading locally to high value of twist angle, will drive consequently to high value of mixity angles and associated high values of  $\Delta K_{II}$  and  $\Delta K_{III}$  as compared to  $\Delta K_I$ . As an example, the macroscopic twist angle was close to  $0^\circ$  for Crack #1, see  $\Psi_1$  for  $1.6 < x < 2$ . mm Figure 6(b), these points corresponding to the maximum FCGR for  $T=0.7$  in Figure 13(c). In addition to this observation, this acceleration of crack growth for  $T=0.7$  corresponds to

a crack orientation on the observed surface, close to the initial orientation of notch, Figure 5(b), leading to a very low value of tilt angle on specimen surface. As a consequence of this orientation of the surface crack, according to macroscopic mode I and II loading, the  $\Delta K_{II}$  should have reached a maximum value, that could decrease the value of  $\Delta K_I$ , Figure 11(a). Thus, a careful analysis of local 3D morphology of crack is needed to determine if the local 3D shape of the crack could explain FCGR oscillations. These observations have also raised the question of the role of local description of anisotropy in 3D, including a detailed analysis of local yielding, in the crack behavior. This issue is particularly complex for Ti6242, where a competition between the scale length of the microstructure heterogeneity and the continuum description of the crack shape takes place. Since, for Ti6242 the microstructure influence is very important, authors have proposed to model explicitly the  $\alpha$  needles to determine local loading [47]. But it remains challenging to model this level of complexity along the whole crack path in 3D.

And last but not least, the chosen  $\Delta K_{eq}$  has enabled to prove that the behavior of the welded specimen was a direct function of the crack tip location within fusion zone or HAZ. Finally, the HAZ-Ti17 and HAZ-Ti6242's respective behavior were very close to Ti17 and Ti6242 base metals under macroscopic combination of mode I and II loading.

## 7. Conclusions

This study aimed to address the influence of laser welding of Ti based alloys on FCGR for multiaxial fatigue loading. Moreover the influence of microstructure in welded Ti based alloys has been established by comparison of behavior in base metals and different areas of the welded material. The main results could be resumed as follows:

- Ti17 exhibited a regular crack path, for equibiaxial as well as for combination of mode I and II loading condition. Nevertheless, the lack of microstructural barrier has led to high FCGR. Furthermore, the regularity of crack path for both tilting and twisting has made the Ti17 specimen a reference case;
- Ti6242 exhibited a predominant influence of microstructure, where large oscillations at the scale length of  $\alpha$  colonies have impeded the FCGR leading to the lowest FCGR under equibiaxial loading. Nevertheless, the microstructural barrier was unable to limit FCGR under macroscopic combination of mode I and II leading to the highest FCGR under mode I + II observed for the different tested materials;
- Laser welded Ti17/Ti6242 microstructure was no longer optimized and has led to high FCGR that was only reaching FCGR measured in base metals when the crack was evolving out of the fusion zone;

- Considering a simple, but relevant, modeling of the 3D crack shape has enabled to stress out the strong coupling between shear modes and resulting FCGR. This SIF analysis has highlighted the strong influence of mode III for macroscopic loading involving mode I+II;
- An equivalent SIF was identified to account for mode mixity on the most homogeneous and continuous case observed for Ti17;
- This equivalent SIF was seen to be fairly able to describe all tested material configurations: base metal Ti17 or Ti6242 and for welded specimen.

### **Acknowledgements**

We would like to thank S. Rix, S. Pierret from Safran Aircraft Engine for providing materials. We gratefully acknowledge useful discussions with E. Gautier (IJL CNRS Université de Lorraine UMR 7198).

## Bibliography

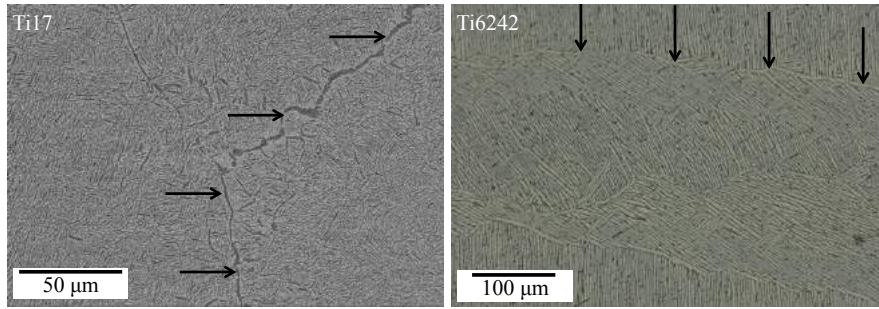
- [1] D. Broek, *Elementary Engineering Fracture Mechanics*, Sijthoff and Noordhoff, 1984.
- [2] H. Ghonem, Microstructure and fatigue crack growth mechanisms in high temperature titanium alloys, *International Journal of Fatigue* 32 (9) (2010) 1448–1460.
- [3] D. Eylon, J. Hall, Fatigue behavior of beta processed titanium alloy imi 685, *Metallurgical Transactions A* 8 (6) (1977) 981–990.
- [4] F. Sansoz, H. Ghonem, Effects of loading frequency on fatigue crack growth mechanisms in  $\alpha/\beta$  ti microstructure with large colony size, *Materials Science and Engineering: A* 356 (1) (2003) 81–92.
- [5] M. Bache, W. Evans, V. Randle, R. Wilson, Characterization of mechanical anisotropy in titanium alloys, *Materials Science and Engineering: A* 257 (1) (1998) 139–144.
- [6] M. Savage, J. Tatalovich, M. Mills, Anisotropy in the room-temperature deformation of  $\alpha$ - $\beta$  colonies in titanium alloys: role of the  $\alpha$ - $\beta$  interface, *Philosophical Magazine* 84 (11) (2004) 1127–1154.
- [7] O. Jin, S. Mall, Effects of microstructure on short crack growth behavior of ti-6al-2sn-4zr-2mo-0.1 si alloy, *Materials Science and Engineering: A* 359 (1) (2003) 356–367.
- [8] F. Sansoz, H. Ghonem, Fatigue crack growth mechanisms in ti6242 lamellar microstructures: Influence of loading frequency and temperature, *Metallurgical and Materials Transactions A* 34 (11) (2003) 2565–2577.
- [9] J. Qiu, X. Feng, Y. Ma, J. Lei, Y. Liu, A. Huang, D. Rugg, R. Yang, Fatigue crack growth behavior of beta-annealed ti-6al-2sn-4zr-xmo ( $x= 2, 4$  and  $6$ ) alloys: Influence of microstructure and stress ratio, *International Journal of Fatigue* 83 (2016) 150–160.
- [10] J. Oh, N. J. Kim, S. Lee, E. W. Lee, Correlation of fatigue properties and microstructure in investment cast ti-6al-4v welds, *Materials Science and Engineering: A* 340 (1) (2003) 232–242.
- [11] J. Fu, Y. Shi, Effect of cracked weld joint and yield strength dissimilarity on crack tip stress triaxiality, *Theoretical and applied fracture mechanics* 25 (1) (1996) 51–57.
- [12] S. Biroasca, J. Buffiere, F. Garcia-Pastor, M. Karadge, L. Babout, M. Preuss, Three-dimensional characterization of fatigue cracks in ti-6246 using x-ray tomography and electron backscatter diffraction, *Acta materialia* 57 (19) (2009) 5834–5847.
- [13] A. Trudel, M. Lévesque, M. Brochu, Microstructural effects on the fatigue crack growth resistance of a stainless steel ca6nm weld, *Engineering Fracture Mechanics* 115 (2014) 60–72.
- [14] M. Abecassis, A. Köster, V. Maurel, Short and long crack growth behavior of welded ferritic stainless steel, *Procedia Structural Integrity* 2 (2016) 3515–3522.
- [15] Y. Ji, S. Wu, G. Yu, Fatigue crack growth characteristics of inertia friction welded ti17 alloy, *Fatigue & Fracture of Engineering Materials & Structures* 37 (1) (2014) 39–49.
- [16] S. Wang, J. Liu, D. Chen, Strain-controlled fatigue properties of dissimilar welded joints between ti-6al-4v and ti17 alloys, *Materials & Design* 49 (2013) 716–727.
- [17] K. Tanaka, Fatigue crack propagation from a crack inclined to the cyclic tensile axis, *Engineering Fracture Mechanics* 6 (3) (1974) 493–507.
- [18] S. Forth, W. Keat, L. Favrow, Experimental and computational investigation of three-dimensional mixed-mode fatigue, *Fatigue & Fracture of Engineering Materials & Structures* 25 (1) (2002) 3–15.
- [19] X. Huang, M. Torgeir, W. Cui, An engineering model of fatigue crack growth under variable amplitude loading, *International Journal of Fatigue* 30 (1) (2008) 2–10.
- [20] Y. Liu, L. Liu, B. Stratman, S. Mahadevan, [Multiaxial fatigue reliability analysis of railroad wheels](#), *Reliability Engineering & System Safety* 93 (3) (2008) 456 – 467, probabilistic Modelling of Structural Degradation. doi:<https://doi.org/10.1016/j.ress.2008.03.001>

[//doi.org/10.1016/j.res.2006.12.021](https://doi.org/10.1016/j.res.2006.12.021).

URL <http://www.sciencedirect.com/science/article/pii/S0951832007000117>

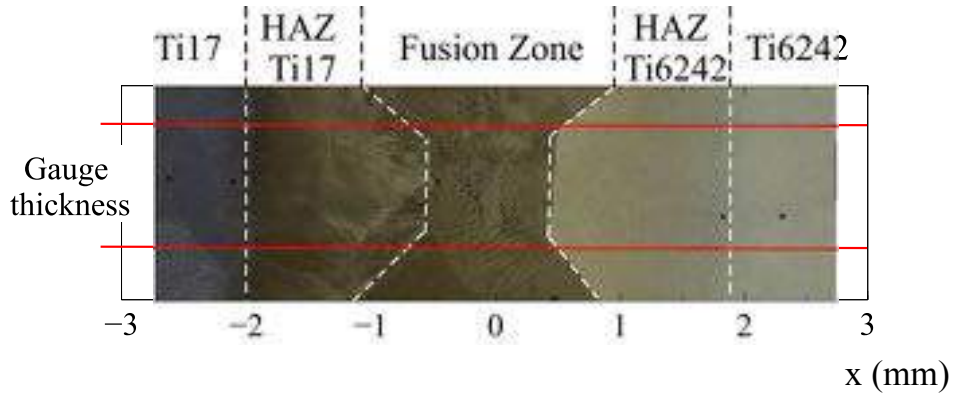
- [21] F. Hourlier, D. McLean, A. Pineau, Fatigue crack growth behaviour of ti-5al-2.5sn alloy under complex stress (mode i+ steady mode iii), *Metals Technology* 5 (1) (1978) 154–158.
- [22] V. Doquet, S. Pommier, Fatigue crack growth under non-proportional mixed-mode loading in ferritic-pearlitic steel, *Fatigue & Fracture of Engineering Materials & Structures* 27 (11) (2004) 1051–1060.
- [23] N. Moës, J. Dolbow, T. Belytschko, A finite element method for crack growth without remeshing, *International journal for numerical methods in engineering* 46 (1) (1999) 131–150.
- [24] S. Bordas, T. Rabczuk, G. Zi, Three-dimensional crack initiation, propagation, branching and junction in non-linear materials by an extended meshfree method without asymptotic enrichment, *Engineering Fracture Mechanics* 75 (5) (2008) 943–960.
- [25] V. Chiaruttini, D. Geoffroy, V. Riolo, M. Bonnet, An adaptive algorithm for cohesive zone model and arbitrary crack propagation, *European Journal of Computational Mechanics/Revue Européenne de Mécanique Numérique* 21 (3-6) (2012) 208–218.
- [26] S. Forth, L. Favrow, W. Keat, J. Newman, Three-dimensional mixed-mode fatigue crack growth in a functionally graded titanium alloy, *Engineering fracture mechanics* 70 (15) (2003) 2175–2185.
- [27] F. Ding, T. Zhao, Y. Jiang, A study of fatigue crack growth with changing loading direction, *Engineering fracture mechanics* 74 (13) (2007) 2014–2029.
- [28] Y. Xiangqiao, D. Shanyi, Z. Zehua, Mixed-mode fatigue crack growth prediction in biaxially stretched sheets, *Engineering fracture mechanics* 43 (3) (1992) 471–475.
- [29] M. Brown, K. Miller, Mode i fatigue crack growth under biaxial stress at room and elevated temperature, *Multiaxial Fatigue*, ASTM STP 853 (1985) 135–152.
- [30] G. Lütjering, Influence of processing on microstructure and mechanical properties of ( $\alpha$ +  $\beta$ ) titanium alloys, *Materials Science and Engineering: A* 243 (1-2) (1998) 32–45.
- [31] J. D. C. Teixeira, B. Appolaire, E. Aeby-Gautier, S. Denis, G. Cailletaud, N. Späth, Transformation kinetics and microstructures of ti17 titanium alloy during continuous cooling, *Materials Science and Engineering: A* 448 (1-2) (2007) 135–145.
- [32] A. Settefrati, E. Aeby-Gautier, M. Dehmas, G. Geandier, B. Appolaire, S. Audion, J. Delfosse, Precipitation in a near beta titanium alloy on ageing: Influence of heating rate and chemical composition of the beta-metastable phase, in: *Solid State Phenomena*, Vol. 172, Trans Tech Publ, 2011, pp. 760–765.
- [33] C. Cheng, B. Yu, Z. Chen, J. Liu, et al., Mechanical properties of electron beam welded dissimilar joints of tc17 and ti60 alloys, *Journal of Materials Science & Technology*.
- [34] S. Hertz-Clemens, Etude d'un composite aéronautique à matrice métallique sous chargements de fatigue: sollicitation mécano-thermique et propagation de fissures, Ph.D. thesis, École Nationale Supérieure des Mines de Paris (2002).
- [35] C. Sarrazin-Baudoux, Abnormal near-threshold fatigue crack propagation of ti alloys: role of the microstructure, *International journal of fatigue* 27 (7) (2005) 773–782.
- [36] G. C. Sih, *Handbook of stress-intensity factors*, Lehigh University, Institute of Fracture and Solid Mechanics, 1973.
- [37] E. Fessler, E. Andrieu, V. Bonnand, V. Chiaruttini, S. Pierret, Relation between crack growth behaviour and crack front morphology under hold-time conditions in da inconel 718, *International Journal of Fatigue* 96 (2017) 17–27.
- [38] H. S. Lamba, the j-integral applied to cyclic loading, *Engineering Fracture Mechanics* 7 (1975) 693–703.
- [39] G. Nikishkov, S. Atluri, Calculation of fracture mechanics parameters for an arbitrary three-dimensional crack, by the equivalent domain integral method, *International journal for numerical methods in engineering* 24 (9) (1987) 1801–1821.

- [40] D. Benziane, V. Chiaruttini, J. Garaud, F. Feyel, R. Foerch, N. Osipov, S. Quillici, J. Rannou, A. Roos, D. Ryckelynck, Z-set/zebulon: une suite logicielle pour la mécanique des matériaux et le calcul de structures, Comptes rendus du 10ème Colloque National en Calcul des Structures, Giens, 2011.
- [41] A. International, A. I. H. Committee, A. I. A. P. D. Committee, Metals Handbook: Properties and selection, Vol. 2, ASM international, 1990.
- [42] O. Gourbesville, Caracterisation par drx de la microstructure d'alliages a base de nickel (718) et a base de titane (ti-17) forges et traites prevision des proprietes mecaniques, Ph.D. thesis, Paris, ENSAM (2000).
- [43] J. Hutchinson, Z. Suo, *Mixed mode cracking in layered materials*, Vol. 29 of Advances in Applied Mechanics, Elsevier, 1991, pp. 63 – 191. doi:DOI:10.1016/S0065-2156(08)70164-9.  
URL <http://www.sciencedirect.com/science/article/B7RNC-4S867PY-7/2/49133e3f26bd5f190114db2a78ea090d>
- [44] C. Wojcik, K. Chan, D. Koss, Stage i fatigue crack propagation in a titanium alloy, Acta Metallurgica 36 (5) (1988) 1261–1270.
- [45] S. Biroasca, J. Buffiere, M. Karadge, M. Preuss, 3-d observations of short fatigue crack interaction with lamellar and duplex microstructures in a two-phase titanium alloy, Acta Materialia 59 (4) (2011) 1510–1522.
- [46] W. Ludwig, J.-Y. Buffière, S. Savelli, P. Cloetens, Study of the interaction of a short fatigue crack with grain boundaries in a cast al alloy using x-ray microtomography, Acta Materialia 51 (3) (2003) 585–598.
- [47] G. Martin, Simulation numérique multi-échelles du comportement mécanique des alliages de titane bêta-métastable ti5553 et ti17, Ph.D. thesis, Ecole Nationale Supérieure des Mines de Paris (2012).

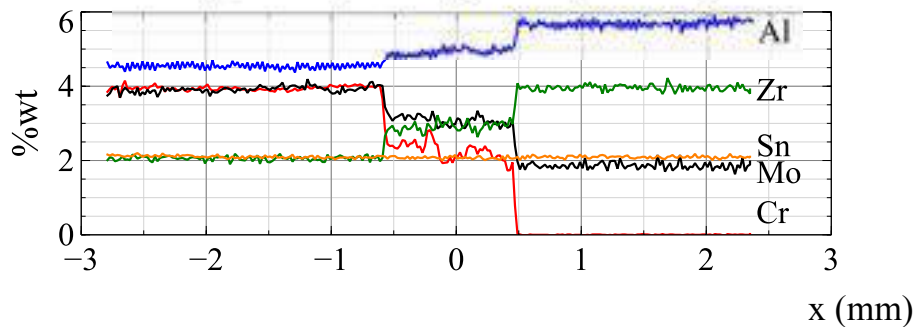


(a) SEM Ti17

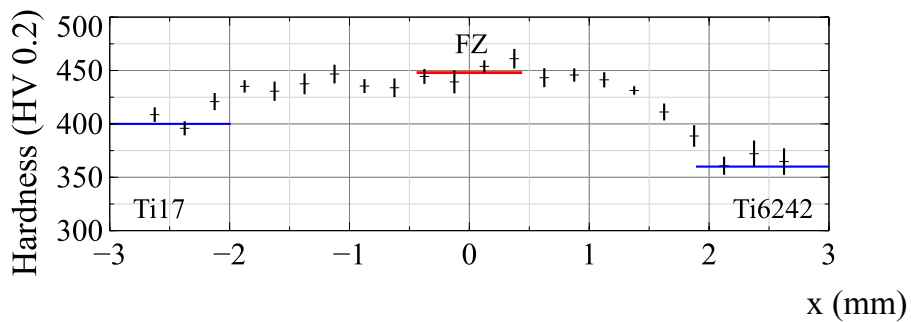
(b) OM Ti6242



(c) OM Ti17-Ti6242



(d) %wt Ti17-Ti6242



(e) HV Ti17-Ti6242

Figure 1: Initial microstructure for (a) Ti17 titanium alloy (SEM) and (b) Ti6242 titanium alloy (OM) where black arrows indicate some prior  $\beta$  grains boundaries. Microstructure (c) welded Ti17-Ti6242 material, cross-section orthogonal to the welding direction (OM). For welded material (d) concentration profile through the welded joint and (e) hardness measurement associated to (c) where cross indicate mean HV value for each x position (vertical bar is sized to standard deviation).  $x$  indicates the abscissa along the cross-section (c).

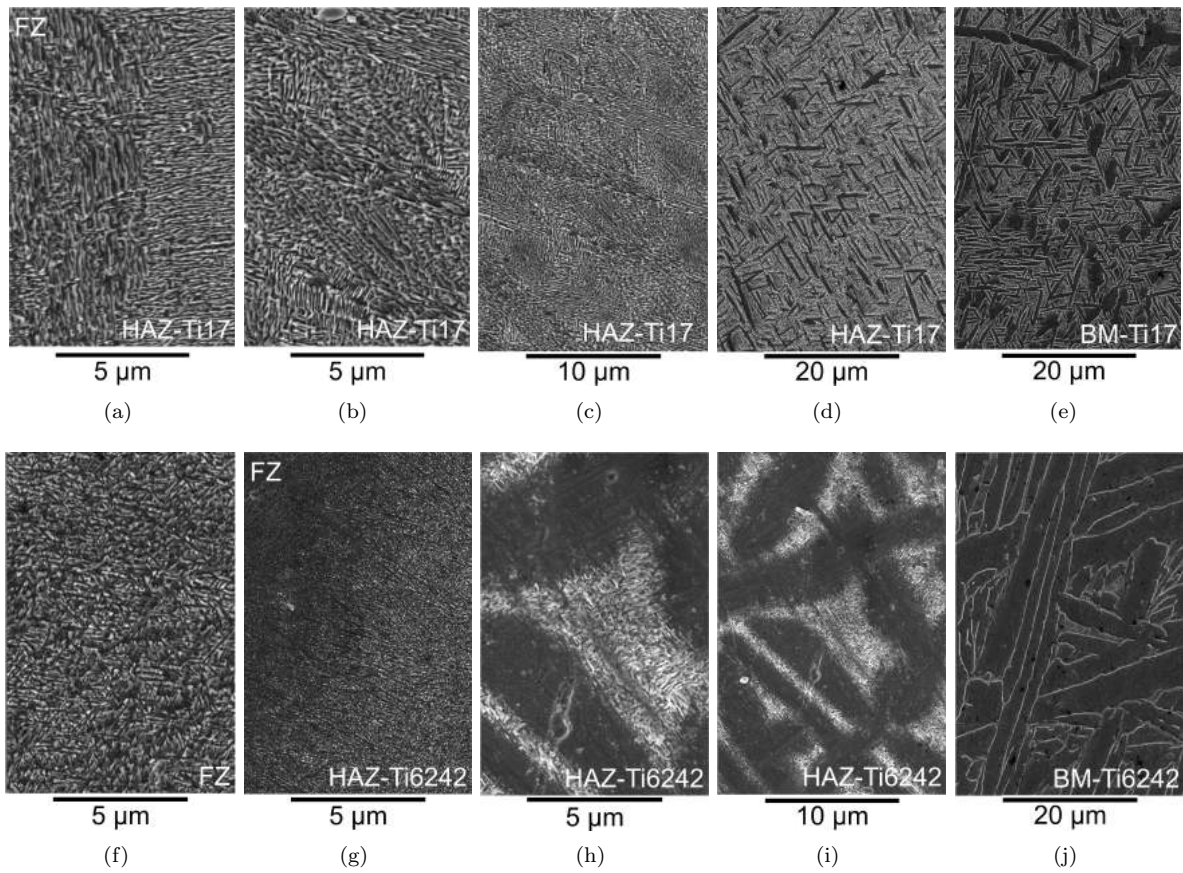


Figure 2: Microstructure of welded Ti17-Ti6242 material : (a) near the interface between FZ and HAZ-Ti17, (b) to (d) within the HAZ-Ti17 progressively reaching (e) the area of BM-Ti17, (b) is a zoom of (c) and (f) within the FZ, (g) near the interface between FZ and HAZ-Ti6242, (g) and (h) within the HAZ-Ti6242 progressively reaching (j) the area of BM-Ti6242, (h) is a zoom of (i).

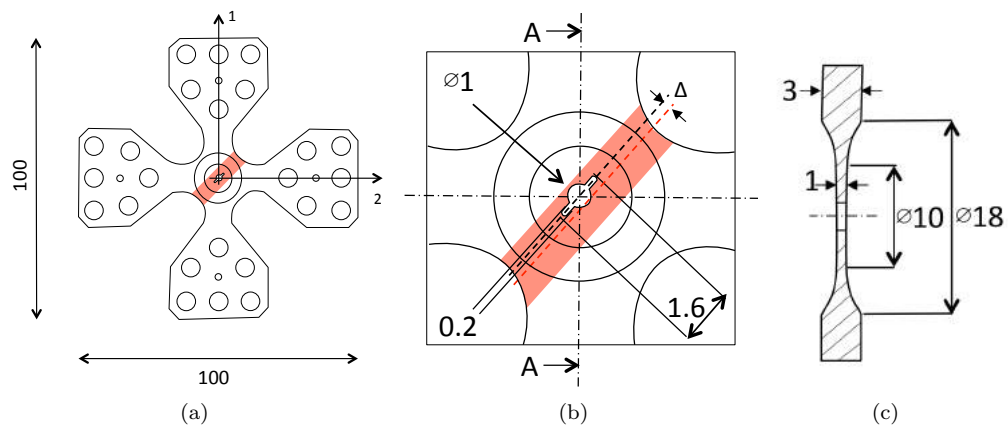


Figure 3: (a) Specimen geometry; red area corresponds to the location of welded joint for welded specimen, (b) detail of the gauge surface and (c) cross section of the gauge surface

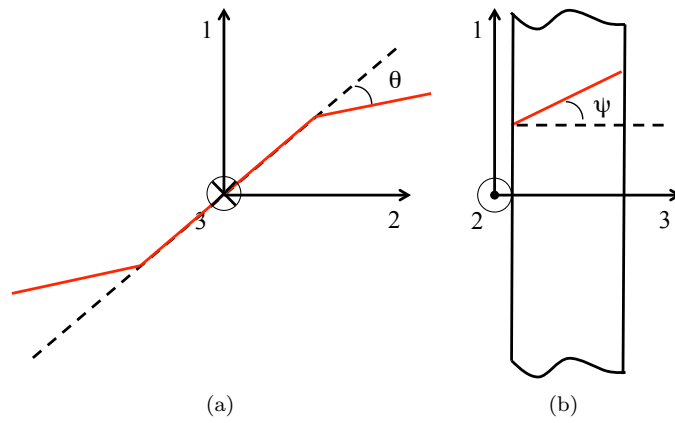
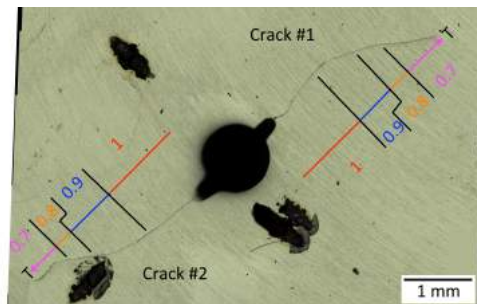
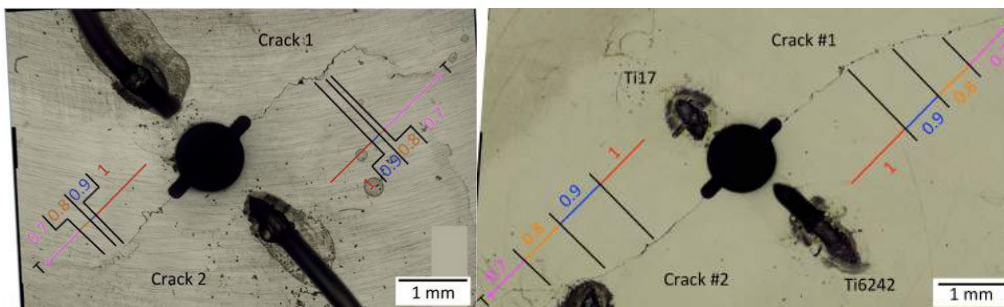


Figure 4: Definition (a) of crack bifurcation by tilt angle,  $\theta$ , and (b) of crack flat to slant deviation by twist angle,  $\psi$ , in the thickness of the specimen (crack is plot in red continuous line).



(a) Ti17



(b) Ti6242

(c) Welded Ti17/Ti6242

Figure 5: Final crack paths (OM) for (a) Ti17 base alloy, (b) Ti6242 base alloy and (c) welded specimens. Arrows indicate the biaxial loading ratio T.

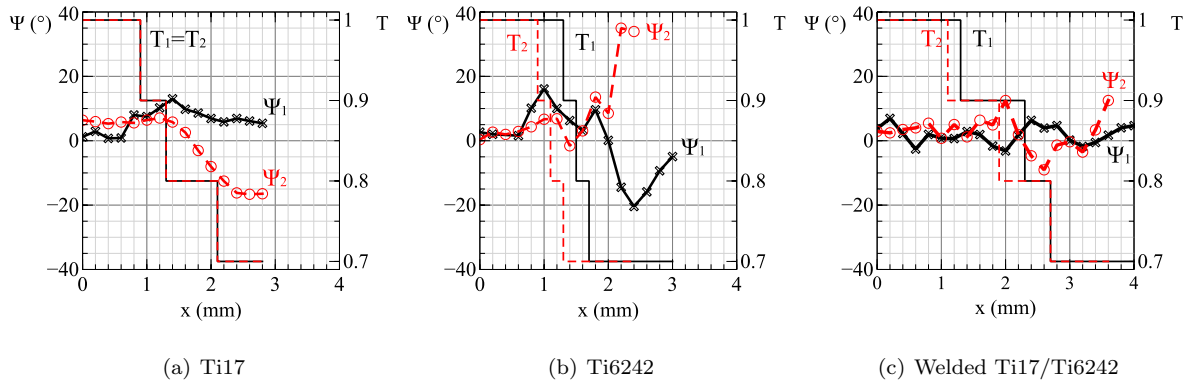
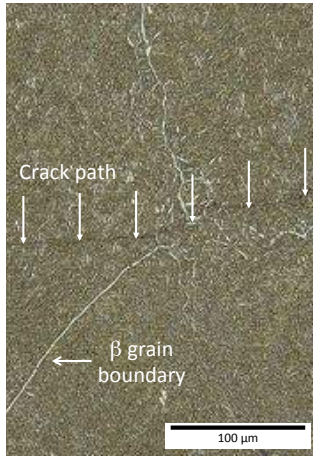
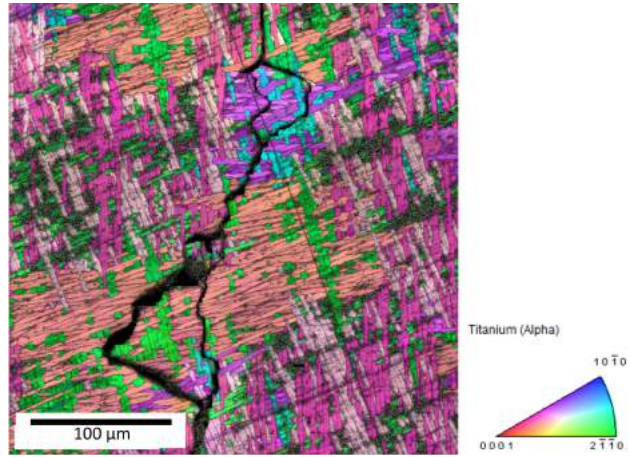


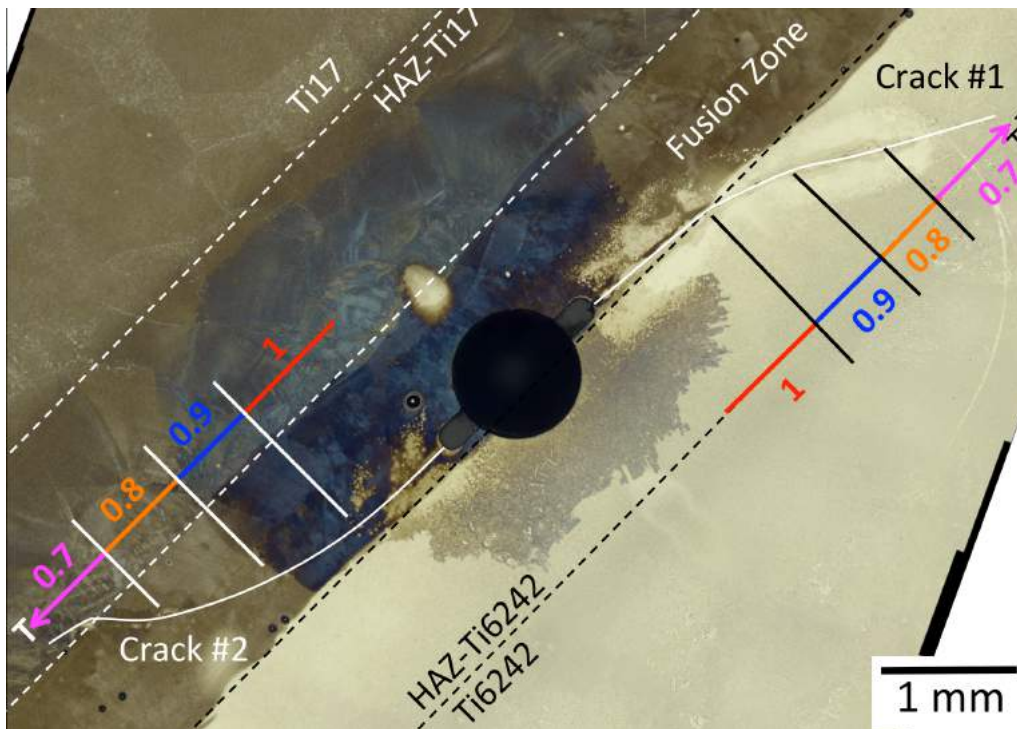
Figure 6: Twist angle evolution,  $\psi$  (symbol and lines, left ordinate) and biaxial loading ratio,  $T$  (continuous and dashed lines, right ordinate) as a function of crack length,  $x$ , for Cracks #1 (continuous black line) and #2 (dashed red lines)



(a) Ti17



(b) Ti6242



(c) Welded Ti17/Ti6242

Figure 7: Microstructure and crack paths for (a) Ti17 base alloy, (b) Ti6242 base alloy and (c) welded specimens.

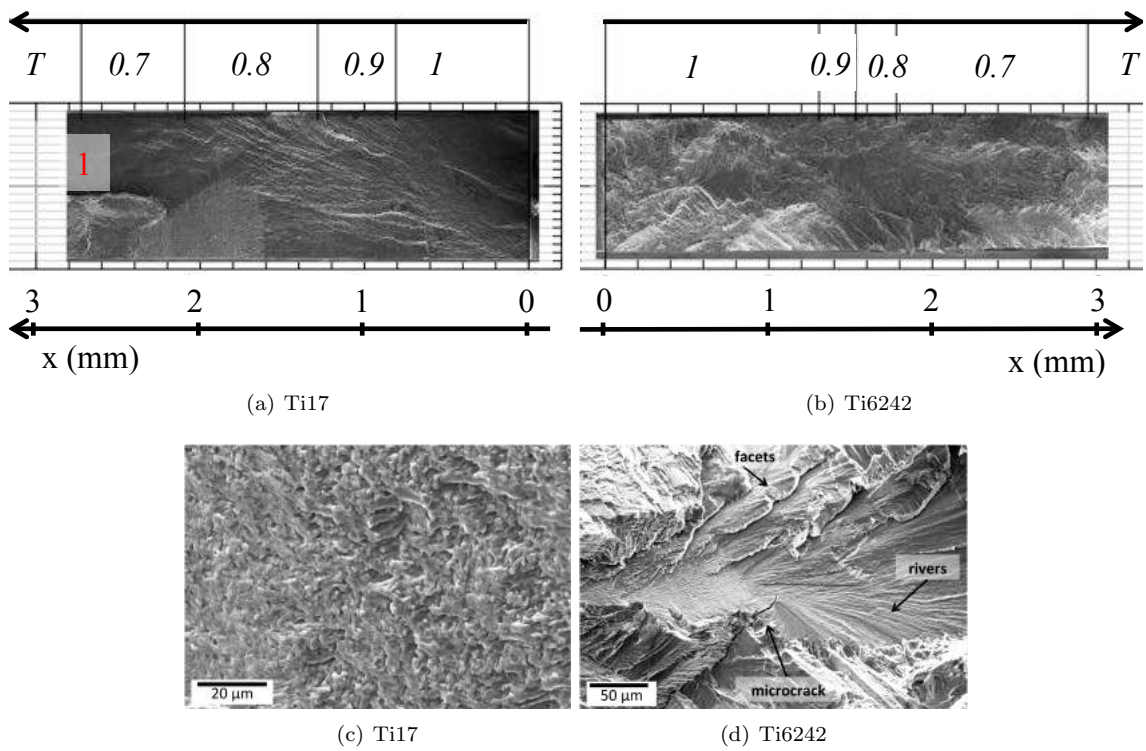
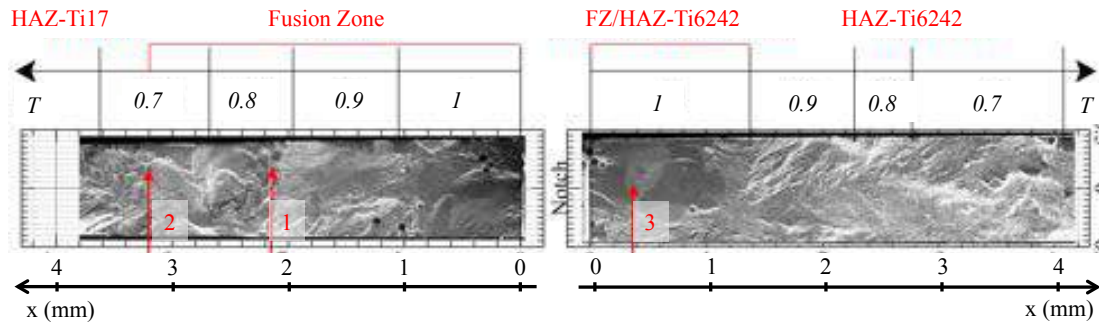
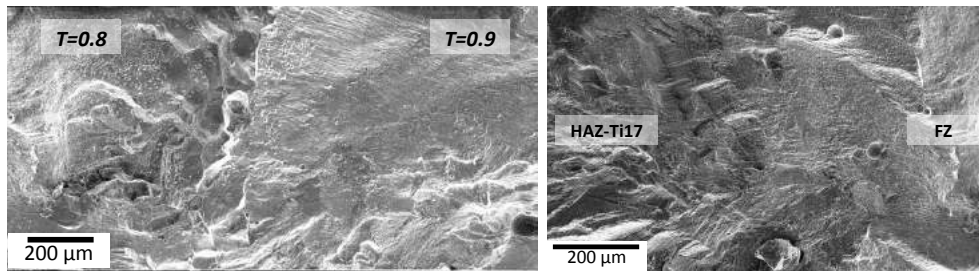


Figure 8: Fractographic observation by SEM for (a) Ti17 and (b) Ti6242;  $x$  is the abscissa and  $T$  the associated biaxiality ratio (resp. below and above cross-sections); details observed on crack surface for (c) Ti17 and (d) Ti6242

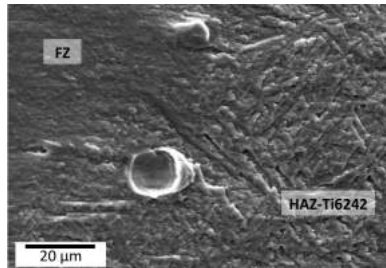


(a) Welded Ti17-Ti6242, Crack #2 (left) and Crack #1 (right)



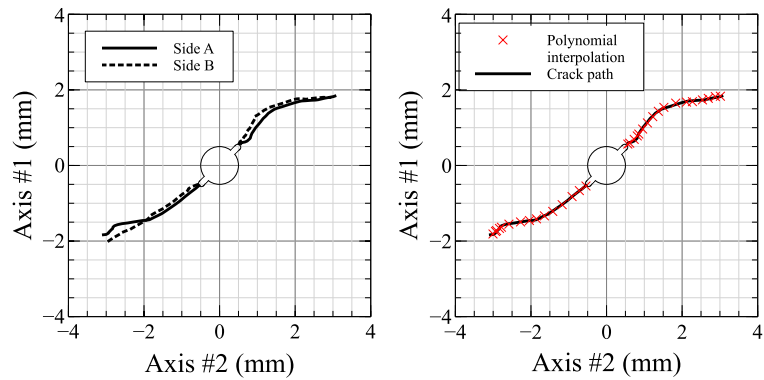
(b) Detail associated to label 1

(c) Detail associated to label 2

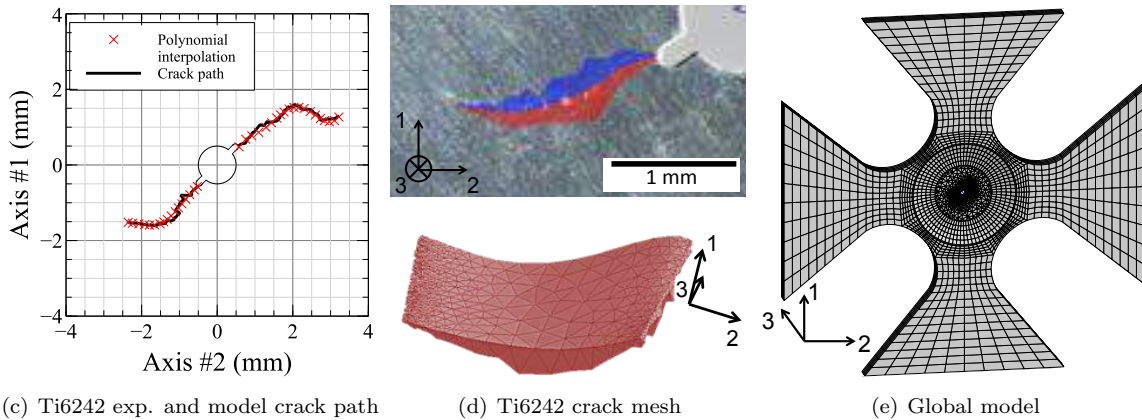


(d) Detail associated to label 3

Figure 9: Fractographic observation by SEM for (a) Ti17-Ti6242 welded specimen and details (b) to (d) corresponding to label 1 to 3 in (a); in (a)  $x$  is the abscissa and  $T$  the associated biaxiality ratio (resp. below and above cross-sections)



(a) Ti17 exp. crack path on both sides (b) Ti17 exp. and model crack path for side A



(c) Ti6242 exp. and model crack path

(d) Ti6242 crack mesh

(e) Global model

Figure 10: (a) crack path observed on both sides of the Ti17 specimen (side A corresponds to Figure 5(a)); (b) and (c) crack shape interpolation of one side of the Ti17 and Ti6242 specimen respectively ; (d) crack shape interpolation on one side of the Ti6242 specimen where contiguous sets of elements have been colored and (e) global model of the specimen

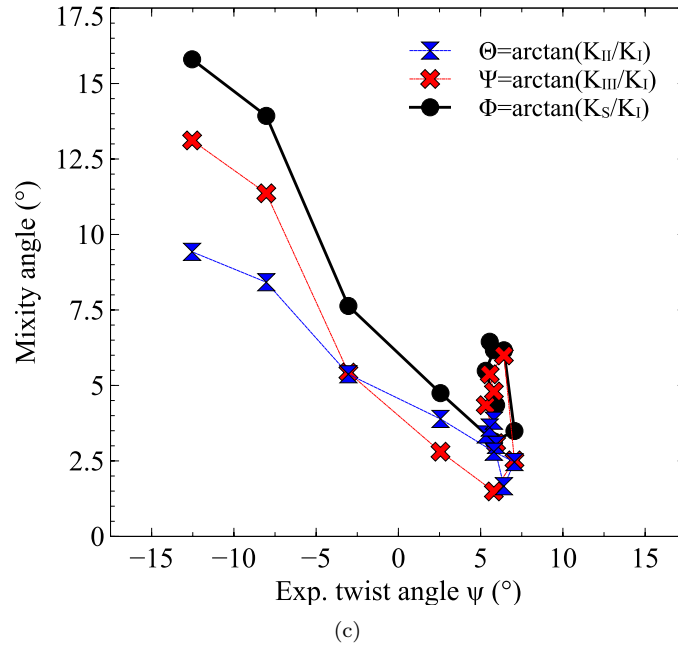
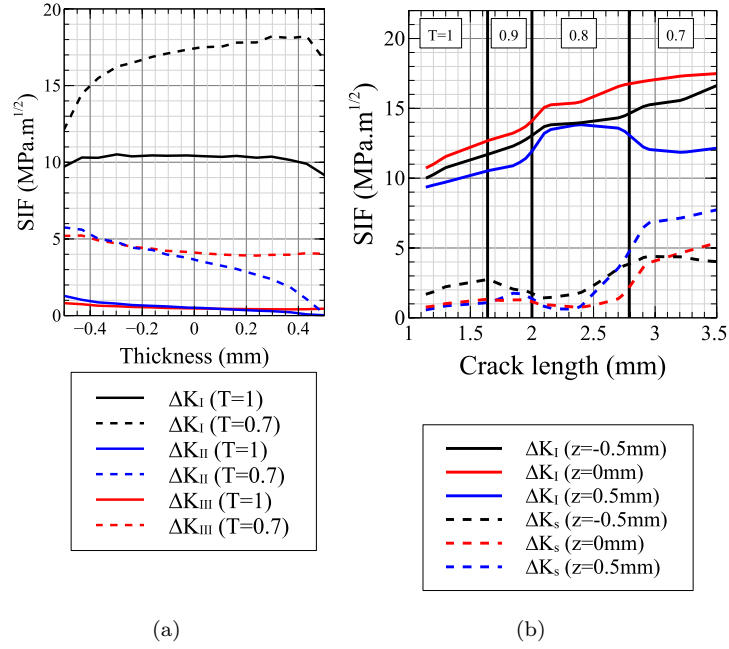
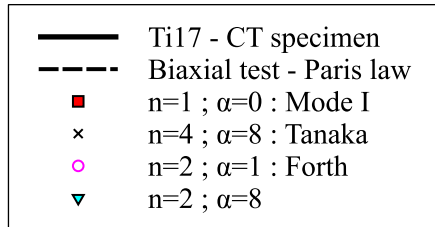
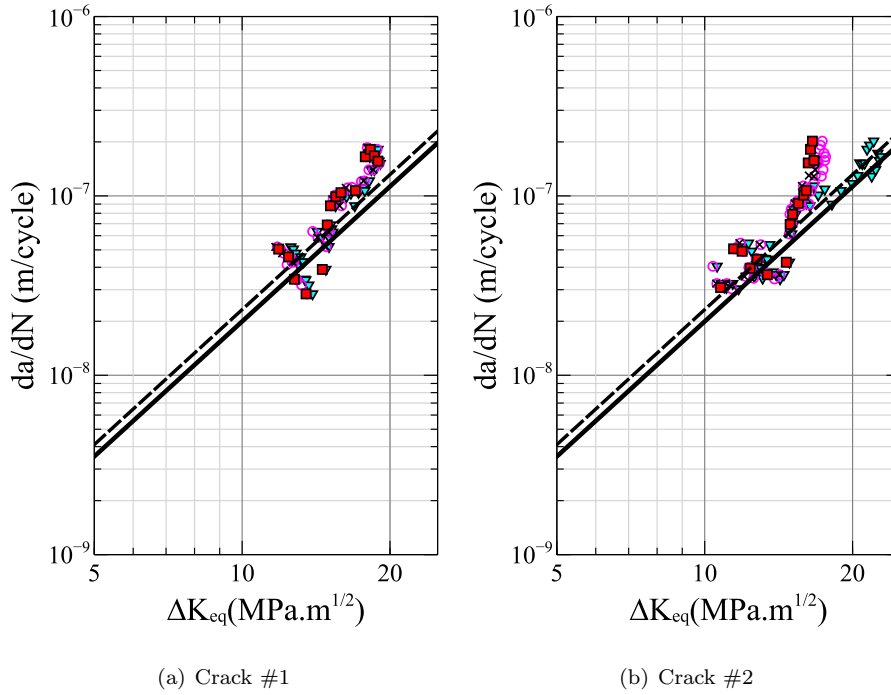


Figure 11: SIF analysis for Ti17 specimen corresponding to Crack #2 in Figure 5(a) (a) SIF amplitude for modes I, II, III for two crack tip locations corresponding to T=1 and T=0.7 respectively (b) evolution of SIF amplitude for mode I,  $\Delta K_I$  and shear mode,  $\Delta K_s$  eq. 3, (c) mode mixity angle function of the twist angle, related to equations 4 to 6



(c) legend

Figure 12:  $\Delta K_{eq}$  tested for Ti17 alloy for pure mode I, Tanaka eq. 11, Forth eq. 14 and proposed  $\Delta K_{eq}$  eq. 16. Continuous line corresponds to Paris law identified with a CT specimen and dashed line corresponds to Paris law identified with biaxial specimen.

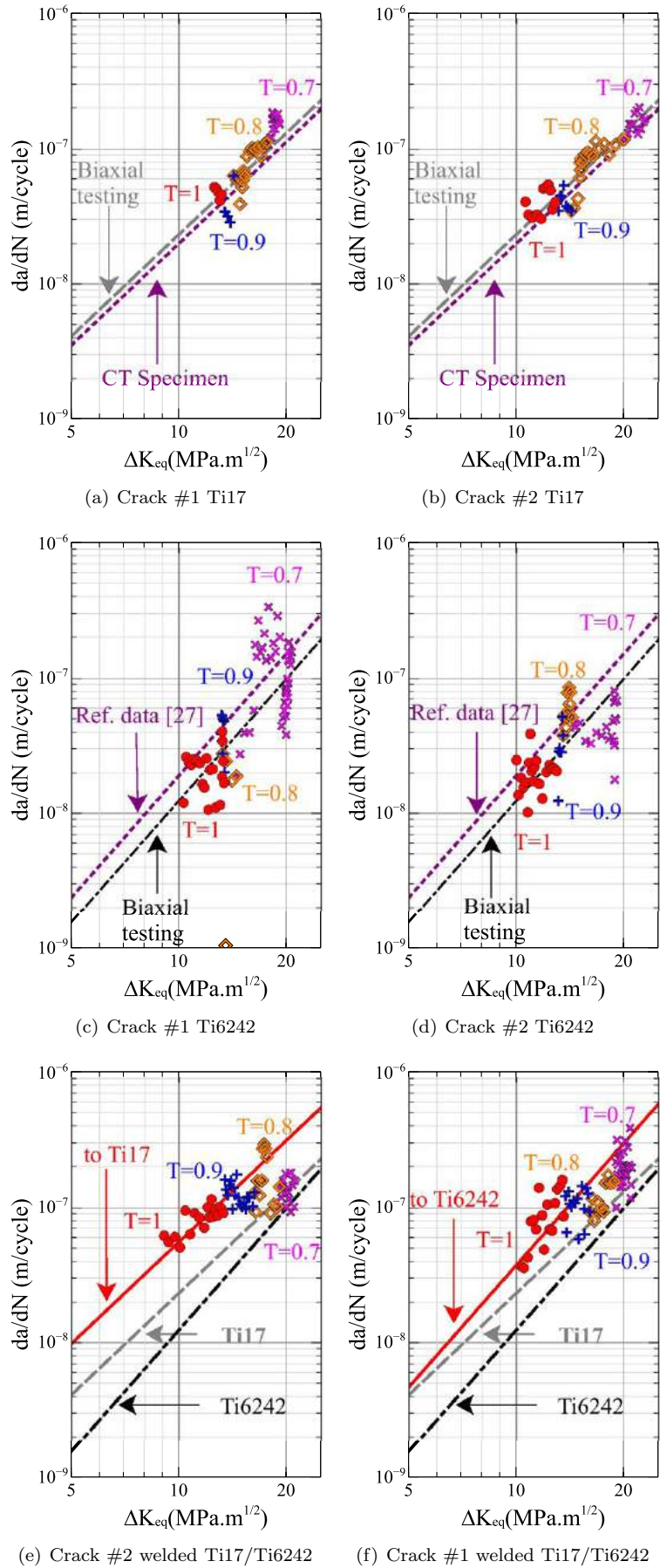


Figure 13: FCGR evolution function of proposed equivalent SIF,  $\Delta K_{eq}$  eq. 16, for each crack front and each tested specimen. Dotted lines correspond to Paris law identified with a CT specimen for Ti17 (resp. from literature data for Ti6242), dashed line (resp. dashed dot line) corresponds to Paris law identified with biaxial specimen for Ti17 (resp. for Ti6242) using proposed  $\Delta K_{eq}$ ,  $\Delta K_{eq}$  eq. 16.